Main Manuscript for

Dynamics of hydraulic and contractile wave-mediated fluid transport during *Drosophila* oogenesis

Authors

Jasmin Imran Alsous[1], Nicolas Romeo[2,†], Jonathan A. Jackson[1,3,†], Frank Mason[4], Jörn Dunkel[5,*], Adam C. Martin[1,*]

Author affiliations

[1] Department of Biology, Massachusetts Institute of Technology, Cambridge, MA, 02139.
[2] Department of Physics, Massachusetts Institute of Technology, Cambridge, MA, 02139.
[3] Graduate Program in Biophysics, Harvard University, Cambridge, MA, 02138.
[4] Vanderbilt-Ingram Cancer Center, Division of Hematology and Oncology, Department of Medicine, Vanderbilt University Medical Center, Nashville, TN, 37232.
[5] Department of Mathematics, Massachusetts Institute of Technology, Cambridge, MA, 02139.
[†] Equal contribution
[*] Corresponding authors: Adam C. Martin and Jörn Dunkel

Email acmartin@mit.edu, dunkel@mit.edu

Abstract

From insects to mice, oocytes develop within cysts alongside nurse-like sister germ cells. Prior to fertilization, the nurse cells' cytoplasmic contents are transported into the oocyte, which grows as its sister cells regress and die. Although critical for fertility, the biological and physical mechanisms underlying this transport process are poorly understood. Here, we combined live imaging of germline cysts, genetic perturbations, and mathematical modeling to investigate the dynamics and mechanisms that enable directional and complete cytoplasmic transport in *Drosophila melanogaster* egg chambers. We discovered that during 'nurse cell (NC) dumping', most cytoplasm is transported into the oocyte independently of changes in myosin-II contractility, with dynamics instead explained by an effective Young-Laplace's law, suggesting hydraulic transport induced by baseline cell surface tension. A minimal flow network model inspired by the famous two-balloon experiment and genetic analysis of a myosin mutant correctly predicts the directionality of transport time scale, as well as its intercellular pattern. Long thought to trigger transport through 'squeezing', changes in actomyosin contractility are required only once cell volume is reduced by ~75%, in the form of surface contractile waves that drive NC dumping to completion. Our work thus demonstrates how biological and physical mechanisms cooperate to enable a critical developmental process that, until now, was thought to be a mainly biochemically regulated phenomenon.

Introduction

Fluid flows play an important role in biological development, from the definition of an organism's body plan (1) and vertebrate organogenesis (2) to cytoplasmic streaming (3) and tissue morphogenesis (4). A widely conserved biofluid mechanical transport process whose dynamics have yet to be uncovered and explained takes place during the development and growth of the egg cell. Across diverse species, oocytes develop within germline cysts alongside nurse-like sister germ cells (5,6). A key juncture in oogenesis occurs when these sister cells transport their cytoplasm to the oocyte prior to fertilization; the oocyte grows as its sister cells regress and die (5-8). Although critical for fertility and early embryonic life, the biological and physical mechanisms underlying this transport process are poorly understood.

Drosophila melanogaster oogenesis is a powerful and relevant process for studies of ovarian development. The *Drosophila* oocyte develops within an egg chamber, a multicellular structure comprising a germline cyst of 16 cells that are interconnected through intercellular bridges called ring canals and covered by an epithelium (Fig. 1A) (9-11). Once the oocyte has grown to ~50% of the egg chamber's volume, all 15 sister germ cells, called nurse cells (NCs), transport their cytoplasm into the oocyte in a process called 'nurse cell dumping'; with a diameter of ~10 μm, the ring canals are large enough to permit passage of most cytoplasmic contents (Fig. 1B; Fig. S1A; Movie S1) (12). It was hypothesized that NC dumping is driven by global cortical contractile forces generated through interactions of non-muscle myosin-2 with actin filaments (henceforth actomyosin). According to this hypothesis, the increased contractility brings about an increase in pressure, causing cytoplasm to be 'squeezed' out of the NCs and into the oocyte (13,14). Mutants in the myosin regulatory light chain (RLC), encoded for by the *spaghetti squash* (*sqh*) gene, do not complete NC dumping (15,16), suggesting a critical role for actomyosin dynamics in this process. However, in the absence of time-resolved quantitative data, actomyosin's role in promoting the complete and directional transport of cytoplasm has remained unclear.

To investigate this process, we used live imaging of egg chambers to reconstruct the collective flow pattern within the 15-cell NC cluster and actomyosin activity during NC dumping. We found that our experimental observations, namely the intercellular directional transport pattern and time scale of this transport phenomenon, in both WT and mutants, are best captured by a networked flow model inspired by the famous two-balloon problem. In contrast to the model of global cortical contraction, our results reveal a different role for actomyosin dynamics during NC dumping: actomyosin surface contraction waves, which have been prominently observed in a variety of biological systems (17-20), allow NC dumping to run to completion. Combined with other recent studies (21), our results demonstrate the importance of hydraulic transport and biological mechanisms in the regulation of multicellular collective behavior during oocyte development in higher organisms.

Results

Using *ex vivo* live imaging of egg chambers with simultaneously labeled membranes (*Ecad::GFP*), myosin-2 (*sqh::mCH*), and cytoplasm (*Clip170::GFP*), we determined the dynamics of NC dumping and corresponding patterns of actomyosin activity. First, through size measurements of the oocyte and the 15 NCs (Fig. S1A to D), we found that NC dumping unfolds over the course of ~100 minutes, a period ~3-fold longer than previously reported through indirect estimates (22,23). We also found that NCs empty ~75% of their volume into the oocyte through spatially uniform shrinkage of the cells, and in the absence of nonuniform cell shape changes and membrane blebbing that imply contractile force generation (Phase I) (24). In contrast, transport of the remaining cytoplasm (Phase II) is accompanied by dynamic and persistent deformations of NC shape and blebbing (Fig. 1, C and D; Fig. S2; Movie S2).

Similarly, we found that NC dumping onset occurs without changes to cortical myosin level and localization pattern as compared to the previous developmental stage. NCs' cortical myosin begins reorganizing from a uniform to a nonuniform dynamic cortical pattern (which increases variation of the cortical myosin signal) only ~40 minutes into NC dumping, coincident with the onset of dynamic NC

shape deformations (Fig. 1E; Movie S3; Fig. S3, A and B); no such changes were observed in control membrane markers (Fig. S3C). We conclude that NC dumping unfolds in two distinct phases, only the latter of which coincides with changes in actomyosin distribution and hallmarks of increased actomyosin contractility, such as plasma membrane blebbing (25).

We therefore explored mechanisms whereby directional intercellular fluid flow can occur in the absence of peristalsis-like cell deformations. To that end, we first determined the spatiotemporal pattern of intercellular cytoplasmic transport and found that NC dumping unfolds in a hierarchical manner that mirrors the NCs' size and arrangement: while the oocyte is the largest cell in the egg chamber, the NCs, which are arranged in four layers (L1-L4; Fig. 2A), also exhibit a descending cell size order according to their distance from the oocyte (26-28). Our data show that NCs directly connected to the oocyte (L1 cells), which are also largest, are first to transport their contents into the oocyte, followed in order by smaller NCs in layers L2-L4 (Fig. 2, B and C).

Driven by our experimental observations, in which smaller cells empty their contents into larger ones prior to changes in myosin localization and cell shape deformations, we developed a networked fluid flow model that was inspired by the two-balloon problem: if two identical balloons inflated to different volumes are allowed to exchange air, the smaller balloon will empty its contents into the larger balloon that grows at its expense (Fig. 2D). This seemingly counter-intuitive phenomenon can be explained by the Young-Laplace law, which states an inverse relationship between pressure p and radius R for a sufficiently large balloon; taking into account the hyperelastic behavior of rubber, the pressure inside the inflated balloon is then given by:

$$p = \frac{2\gamma}{R}\left(1 - \left(\frac{R_0}{R}\right)^6\right) \tag{1}$$

where R_o is the radius of the uninflated balloon and γ is its surface tension (Fig. 2D) (29,30). To apply this description to our biological system, we assumed that the cells are roughly spherical (31) and that cell cortices are incompressible and adequately described by a passive neo-Hookean material under static loading (32) (*Methods*). The two-balloon problem is then readily extended to the germline cyst that can

be represented as a 16-cell network (Fig. 2E), where the pressure-driven flux J_{ij} from cell j to i through a cylindrical ring canal of radius r_{ij} and length L is given by:

$$J_{ij} = G_{ij}(p_j - p_i) \tag{2}$$

with a hydraulic conductance $G_{ij} \propto r_{ij}^4/L$ for Poiseuille-type flow (33). The effective cell surface tension in this description arises from the contributions of both in-plane tension of the plasma membrane and actomyosin cortical tension. Using experimentally determined cell sizes at onset of NC dumping as initial conditions (27), we numerically solved the transport equations for the evolution of cell volumes V_i in the 16-cell tree:

$$\frac{dV_i}{dt} = \sum_{\langle i,j \rangle} J_{ij} = \sum_{\langle i,j \rangle} G_{ij}(p_j - p_i) \tag{3}$$

where the sum runs over connected cell neighbors i and j.

Despite its minimal character, the flow-network model robustly captures qualitatively essential features of the experimentally observed transport dynamics (Fig. S4, A and B; *Methods*). Specifically, the model correctly predicts both the hierarchical pattern of intercellular transport and timescale of NC dumping (Fig. 2F). By also accounting for natural cell-to-cell variability in effective cell surface tension (34), the proposed model successfully captures experimentally observed complex transport patterns along the 16-cell tree. For example, our data show the L4 NC transiently increasing in size during NC dumping, which can occur if the L3 cell to which it is connected shrinks sufficiently such that it becomes smaller than the L4 cell. Such transient back flow away from the oocyte is a feature of NC dumping that has been documented before (35) and is predicted by our model (Fig. S4C, Movie S4).

An insight provided by the model is the high sensitivity of intercellular transport to changes in ring canal size through quartic scaling of the hydraulic conductance. By reconstructing ring canal growth dynamics, we show that ring canals reach approximately 10-fold their initial size throughout oogenesis, consistent with previous studies (12), but also that they do so rapidly prior to the onset of NC dumping (Fig. S5A). It is therefore possible that this an increase in ring canal size sharply accelerates cytoplasmic

118 transport from nurse cells into the oocyte at the onset of NC dumping (Fig. S5B). NC dumping onset is
119 however likely to be affected by other factors as well, such as interactions between the follicle cells and
120 the germline, or external cues.

121 Our model and the Young-Laplace law predict that lowering of the effective NC surface tension
122 will slow down the rate of intercellular transport but will not affect transport directionality or hierarchical
123 order. Cell surface tension depends on an actomyosin cortex and it can be reduced by inhibiting myosin
124 (36). Therefore, to test how transport is affected by reducing surface tension, we quantified the
125 spatiotemporal pattern of NC dumping in a mutant in the myosin RLC, encoded by *spaghetti squash*
126 (*sqh*). sqh^1 mutant germline clones reduce *sqh* mRNA and protein levels by ~90% (37,38). We found that
127 while Sqh-depleted germline cysts are 'dumpless', i.e., do not complete NC dumping (Fig. 2G) (15), the
128 hierarchical transport pattern observed in WT is largely maintained (Fig. 2, H and I; Movie S5). However,
129 NC dumping in sqh^1 mutants proceeded more slowly (Fig. 2I, inset). These results showed that myosin
130 contributes to the baseline level of cortical tension, but not to the direction or order of intercellular
131 cytoplasmic transport, which is consistent with myosin activity not changing in Phase I of transport.

132 Despite the fact that transport of cytoplasm is initiated in sqh^1 mutant egg chambers, NC dumping
133 is not completed in these mutants, suggesting that actomyosin and its regulation are important. Indeed,
134 live imaging of egg chambers with labeled myosin (*sqh::mCH*) and actin (*F-tractin::TdTomato* and
135 *Utr::GFP*) demonstrated that actomyosin is highly dynamic during Phase II of NC dumping. Myosin
136 exhibits a diversity of spatiotemporally organized cortical waves, such as colliding myosin wave fronts,
137 rotating cortical bands, and myosin rings travelling between the cell's poles, which lead to local and
138 dynamic NC shape deformations, rather than isotropic contractions of the entire cell (Fig. 3, A to E;
139 Movie S6). We also found that actomyosin waves in the NCs travel at ~0.3 μm/s, a speed comparable to
140 that of Rho-actin contraction waves observed in frog and starfish oocytes and embryos (17). Notably, the
141 intercellular pattern of actomyosin wave onset mirrors that of cytoplasmic transport, starting in NCs
142 closer to the oocyte, i.e., those that shrink first, before appearing in NCs further away (Fig. 3F).

143 Dynamic actomyosin behaviors like those observed here are regulated through RhoA activation
144 and inhibition (39-41). RhoA is a small GTPase activated by guanine nucleotide exchange factors (GEFs)
145 and inhibited by GTPase-activating proteins (GAPs) (42,43). Binding to downstream effectors, such as
146 the Rho-associated and coiled-coil kinase (ROCK; Rok in *Drosophila*), results in increased contractility
147 through myosin RLC phosphorylation (Fig. 3G) (44-46). Our data show that, similar to myosin, Rok,
148 Utrophin, and F-Tractin exhibit wave-like behavior (Fig. S6, A to C; Movie S7), suggesting that dynamic
149 RhoA regulation, rather than constitutive caspase cleavage-mediated activation of Rok (47), underlies
150 myosin's dynamics. Furthermore, through a genetic screen (40), we identified RhoGAP15B, the
151 *Drosophila* homolog of ARAP1/3, as a critical regulator of wave dynamics; the RhoGAP domain of the
152 human RhoGAP15B homolog exhibits highest specificity towards RhoA (48), consistent with
153 RhoGAP15B regulating actomyosin contractility. We found that while RhoGAP15B depletion in the
154 germline cyst led to a 'dumpless' phenotype (Fig. 3H), onset of NC dumping and the time scale of Phase
155 1 transport was unaffected (Fig. 3I). The hierarchical pattern of Phase I transport was also largely
156 unaffected, although there was greater variability between the timing of L1 and L2 in knockdown egg
157 chambers (Fig. 3I). Instead, RhoGAP15B depletion disrupted myosin wave dynamics and concomitant
158 cell-scale shape deformations otherwise observed during Phase II in WT: cells displayed erratic myosin
159 activity associated with smaller and more transient cell protrusions (Fig. 3, J and K; Movie S8). We
160 confirmed that incomplete NC dumping in RhoGAP15B knockdowns is not attributable to obstructed or
161 diminished ring canal sizes, or disrupted actin cables (Fig. S7) (49). These data suggest that incomplete
162 cytoplasmic transport in RhoGAP15B knockdowns is due to disrupted wave dynamics in Phase II of NC
163 dumping.

164 A clue to actomyosin's role in completing NC dumping came from directly visualizing inter- and
165 intracellular cytoplasmic flow using reflection-mode microscopy. Following actomyosin wave onset and
166 concomitant NC shape deformations, cytoplasm was observed flowing through spaces between NC nuclei
167 and membranes and completing multiple revolutions around the large polyploid nucleus as intercellular
168 anterior-to-posterior transport continued (Fig. 4, A and B; Movie S9). In contrast, intracellular flow in

RhoGAP15B knockdowns appeared erratic and lacked the persistent radial motions around NC nuclei necessary for bringing cytoplasm in contact with a ring canal (Fig. 4, C and D). As a result, RhoGAP15B knockdowns exhibited interrupted anterior-to-posterior intercellular flow, repetitive and more frequent transport of cytoplasm away from the oocyte (Fig. 4, E and F; Movie S10), a greater degree of layer 4 expansion (Fig. 3I), and incomplete NC dumping. Given that actomyosin waves first appear in a nurse cell once it has emptied most of its cytoplasmic contents (Fig. S2E), we propose that wave-mediated NC deformations enable continued transport by dynamically creating spaces between plasma membranes and nuclei in shrunken NCs. This creates a transient path allowing cytoplasm to flow past nuclei from anterior to posterior ring canals. Cytoplasmic transport into the oocyte can then run to completion.

Discussion

The above analysis presents joint experimental and theoretical work that addresses a longstanding question concerning the origin and regulation of multicellular collective behavior during oocyte development: How do support germ cells in a germline cyst directionally transport the entirety of their cytoplasm into the future egg cell before undergoing cell death? Our experiments and theory show that baseline surface tension and differential cell size provide robust and highly tunable fluid-mechanical control over directional intercellular cytoplasmic flow and that subsequent wave-like actomyosin contractions are essential to complete transport (Fig. S8). These findings contrast with previous hypotheses for NC dumping, which assumed that cytoplasm is driven out of the NCs through a global increase in pressure mediated through upregulated cytoskeletal force generation (29), with increases in actomyosin contractility at the onset of NC dumping (13). Such a model however does not mechanistically explain the directionality and hierarchical flow pattern that is observed during NC dumping; importantly, our data show that changes in actomyosin distribution and concomitant membrane blebbing do not occur until the NCs have emptied most of their cytoplasmic contents into the oocyte. The above analysis thus highlights the complementary importance of physical and biological mechanisms in achieving directed intercellular fluid transport during oogenesis. This study adds to the growing list of

195 examples where hydrodynamics plays a critical role in development (1-4). Lastly, this work also
196 uncovers a diversity of myosin wave-like behaviors and a previously unknown function for excitable
197 actomyosin dynamics as one of the final facilitators of material transfer between sister germ cells, thereby
198 expanding the repertoire of roles played by surface cortical waves in development (17-20).
199

200 **Materials and Methods**

201 All experimental data are available in the main text or the Supplementary Information. Experimental
202 protocols are described in the SI Text. The strains and genetic crosses used in this study are in Table S1.
203 We used FIJI and Bitplane's Imaris to analyze our images and movies, and Matlab for aligning data and
204 generating plots. Measurements and sample sizes are recorded in Table S2. The code used for numerical
205 simulations is available on a public repository at https://github.com/NicoRomeo/balloon-dynamics. A
206 summary of the initial conditions and adjustable parameters is given in Table S3.
207

208 **Immunofluorescence and antibodies**. Ovaries were extracted through manual dissection. Flies were
209 raised under standard conditions at 25°C and dissected using an established protocol (50). Ovaries from
210 well-fed adult flies were dissected and fixed in 4% (wt/vol) paraformaldehyde at room temperature for 20
211 minutes and stained with primary antibodies: rat anti-E-cadherin (1:500, Developmental Studies
212 Hybridoma Bank (DSHB)), rabbit anti-PTyr (1:500, Santa Cruz Biotechnology) and mouse anti-NPC
213 (1:500, Abcam). We used goat anti-rat 647nm, goat anti-rabbit 568nm and goat anti-mouse 488nm as
214 secondary antibodies diluted at 1:300. Phalloidin-Alexa-647 (Life Technologies), diluted 1:1000, was
215 used. Samples were mounted in a 50-50 mixture of Aqua-Poly/Mount (Polyscience) and RapiClear 1.47
216 (an optical clearing medium from SunJin Lab Co.).
217

218 **Long-term live imaging**. We used a modified version of the Prasad et al. (2007) protocol for live
219 imaging of dissected egg chambers (51). *Ex vivo* culturing of egg chambers took place. Ovaries from ~2-5
220 flies were dissected in Schneider's *Drosophila* media (ThermoFisher SKU #21720-001) that was also

221 used for *ex vivo* culturing; the separated egg chambers were then transferred to a MatTek dish (MatTek
222 #P35G-1.5-10-C) containing 200 µL of media. Imaging took place on an inverted microscope while
223 leaving the lid on the dish to prevent drying. For outlining membranes in the absence of a fluorescent
224 membrane reporter, CellMask deep red plasma membrane stain (Invitrogen #C10046) was added to
225 Schneider's mix (1:1000).
226
227 **Microscopy**. Imaging was performed on a Zeiss LSM 710 point scanning confocal microscope with a 25x
228 or 40x/1.2 Apochromat water objective lens, a 10x dry lens, an argon ion, 561 nm diode, 594 nm and 633
229 HeNe lasers, and the Zen software. Pinhole settings ranged from 1 – 2.5 Airy units. For two-colour live
230 imaging, band-pass filters were set at ~490 – 565 nm for GFP and ~590 – 690 nm for mCH. For three-
231 colour imaging, band-pass filters were set at ~480 – 560 nm for GFP, ~580 – 635 nm for Alexa Fluor
232 568, and ~660 – 750 nm for Alexa Fluor 647. Imaging using confocal reflection mode was performed by
233 setting the detection to the excitation wavelength, i.e. 488 or 561 nm, and using a mirror instead of a
234 dichroic in the beam path. For live imaging of fluorescent reporters, stacks of 20-60 slices and a z-spacing
235 of 2-3 µm were acquired in succession without delay, setting the bottom surface of the egg chamber that
236 faces the cover slip in the MatTek dish or the slide as the last slice, and the first slice as the deepest
237 visible optical plane in the egg chamber. For live imaging using reflection-mode microscopy, a single
238 slice was imaged at a frame rate of ~0.4-0.9 s/frame in succession. Both modes of imaging took place
239 over the course of ~0.5-3 hours.
240
241 **Genetic screen for RhoGAP dumping mutants.** Standard *Drosophila* genetic techniques were utilized
242 to genetically move together tagged proteins or to stimulate transcription of a reporter gene under UAS
243 control through GAL4 expression. This screen was performed to identify maternal effect phenotypes for
244 Rho GAPs, as previously described (40). Briefly, virgins for 22 *Drosophila* RhoGAP shRNA lines were
245 crossed to mat67,15 drivers with fluorescent markers and egg phenotype (i.e., change in egg size) was
246 scored using a dissecting microscope before imaging gastrulation by confocal. UAS hairpin RNA's were

247 created by the Transgenic RNAi Project at Harvard Medical School (52). Only one of these lines
248 (RhoGAP15B, HMJ02093) gave rise to smaller, 'dumpless' eggs.
249

250 **Acknowledgements**

251 We thank Stefan Muenster (Max Planck Institute, Dresden) and Wendy Salmon (Whitehead Institute,
252 Keck Microscopy Facility) for advice regarding use of reflection-mode microscopy. We thank Clint Ko
253 and Jaclyn Camuglia for assistance with experiments, and Alexander Mietke for discussions on wave-
254 driven cytoplasmic flows. We also thank Stanislav Y. Shvartsman and Miriam Osterfield for comments
255 on the manuscript. This work was supported by the Molecular Biophysics Training Grant (National
256 Institute of General Medical Sciences, T32 GM008313) (J.J.), a Complex Systems Scholar Award from
257 the James S. McDonnell Foundation (J.D.), the Robert E. Collins Distinguished Scholarship Fund (J.D.) ,
258 and National Institute of General Medical Sciences grant R01-GM125646 (A.C.M).
259

260 **Author contributions**

261 J.I.A. conceptualized the project. J.I.A. and A.C.M. designed the experimental pipeline. J.I.A. and J.J.
262 performed the experiments with input from N.R., J.D., and supervision by A.C.M. J.I.A and J.J. analyzed the
263 experimental data. J.J. developed the computational framework for quantitative analysis of NC dumping
264 dynamics. J.D. and N.R. developed the computational model. N.R. performed simulations, for which J.I.A. and
265 J.J. provided data. F.M. performed the genetic screen that identified RhoGAP15B as an essential GAP for NC
266 dumping. J.I.A. wrote the first draft of the paper. All authors discussed and revised the manuscript.
267

268 **References**

269 1. S. Nonaka, H. Shiratori, Y. Saijoh, H. Hamada, Determination of left-right patterning of the mouse
270 embryo by artificial nodal flow. *Nature* ***418***, 96-99 (2002).
271 2. A.G. Kramer-Zucker, et al., Cilia-driven fluid flow in the zebrafish pronephros, brain and Kupffer's
272 vesicle is required for normal organogenesis. *Development* ***132***, 1907-1921 (2005).

273 3. S. Ganguly, L. S. Williams, I. M. Palacios, R. E. Goldstein, Cytoplasmic streaming in *Drosophila*
274 oocytes varies with kinesin activity and correlates with the microtubule cytoskeleton architecture.
275 *Proc. Natl. Acad. Sci. USA.* ***38***, 15109-15114 (2012).
276 4. B. He, K. Doubrovinski, O. Polyakov, E. Wieschaus. Apical constriction drives tissue-scale
277 hydrodynamic flow to mediate cell elongation. *Nature* ***508***, 392-396.
278 5. M.E. Pepling, M. de Cuevas, A.C. Spradling, Germline cysts: a conserved phase of germ cell
279 development? *Trends Cell Biol.* ***9***, 257-262 (1999).
280 6. W. H. Telfer, Development and physiology of the oocyte-nurse cell syncytium. *Adv. Insect Physiol.*
281 ***11***, 223-319 (1975).
282 7. V.K. Jenkins, A.K. Timmons, K. McCall, Trends in Diversity of cell death pathways: insight from the
283 fly ovary. *Trends Cell Biol.* ***23***, 567-574 (2013).
284 8. L. Lei, A.C. Spradling, Mouse oocytes differentiate through organelle enrichment from sister cyst
285 germ cells. *Science* ***352***, 95-99 (2016).
286 9. R. Bastock, D. St Johnston, *Drosophila* oogenesis. *Curr. Biol.* ***18***, R1082-1087 (2008).
287 10. R.C. King, Ed., *Ovarian Development in Drosophila melanogaster*. (Academic Press, New York,
288 NY, 1970).
289 11. A.C. Spradling, "Developmental genetics of oogenesis" in *The Development of Drosophila*
290 *melanogaster*, M. Bate, A. Martinez Arias, Eds. (Cold Spring Harbor Press, Plainview, NY, 1993)
291 vol. 1, pp. 1-70.
292 12. W.E. Theurkauf, T.I. Hazelrigg. *In vivo* analyses of cytoplasmic transport and cytoskeletal
293 organization during *Drosophila* oogenesis: characterization of a multi-step anterior localization
294 pathway. *Development* ***125***, 3655-3666 (1998).
295 13. P. Jordan, R. Karess. Myosin light chain-activating phosphorylation sites are required for oogenesis in
296 *Drosophila*. *J. Cell Biol.* ***139***, 1805-1819 (1997).
297 14. H.O. Gutzeit, R. Koppa (1982). Time-lapse film analysis of cytoplasmic streaming during late
298 oogenesis of *Drosophila*. *J. Embryol. Exp. Morphol.* ***67***, 101-111 (1982).

15. S. Wheatley, S. Kulkarni, R. Karess, *Drosophila* nonmuscle myosin II is required for rapid cytoplasmic transport during oogenesis and for axial nuclear migration in early embryos. *Development* ***121***, 1937-1946 (1995).
16. K.A. Edwards, D.P. Kiehart, *Drosophila* nonmuscle myosin II has multiple essential roles in imaginal disc and egg chamber morphogenesis. *Development* ***122***, 1499-1511 (1996).
17. W.M. Bement, et al., Activator-inhibitor coupling between Rho signaling and actin assembly makes the cell cortex an excitable medium. *Nat. Cell Biol.* ***17***, 1471-1483 (2015).
18. V.E. Deneke et al. Self-organized nuclear positioning synchronizes the cell cycle in *Drosophila* embryos. *Cell* ***177***, 925–941 (2019).
19. J. Bischof *et al*. A cdk1 gradient guides surface contraction waves in oocytes. *Nat. Comm.* ***8***, 849 (2017).
20. A.C. Martin, M. Kaschube, E.F. Wieschaus. Pulsed contractions of an actin-myosin network drive apical constriction. *Nature* ***457***, 495–9 (2009).
21. N. T. Chartier et al., A hydraulic instability drives the cell death decision in the nematode germline. bioRxiv doi: 10.1101/2020.05.30.125864.
22. J. David, J. Merle, A reevaluation of the duration of egg chamber stages in oogenesis of *Drosophila melanogaster*. *Drosophila Inf. Serv.* ***43***, 122 (1968).
23. H. Lin H, A.C. Spradling, Germline stem cell division and egg chamber development in transplanted *Drosophila* germaria. *Dev. Biol.* ***159***, 140-152 (1993).
24. G. T. Charras, A short history of blebbing. *J. Microsc.* ***231***, 466-478 (2008).
25. G.T. Charras, M. Coughlin, T. J. Mitchison, L. Mahadevan, Life and times of a cellular bleb. *Biophys. J.* ***94***, 1836-1853 (2008).
26. J. Imran Alsous, P. Villoutreix, N. Stoop, S.Y. Shvartsman, J. Dunkel. Entropic effects in cell lineage tree packings. *Nat. Phys.* ***14***, 1016-1021 (2018).
27. J. Imran Alsous, P. Villoutreix, A.M. Berezhkovskii, S.Y. Shvartsman, Collective growth in a small cell network. *Curr. Biol.* ***27***, 2670-2676 (2017).

325 28. E.H. Brown, R.C. King, Studies on the events resulting in the formation of an egg chamber in
326 *Drosophila melanogaster*. *Growth* ***28***, 41-81 (1964).
327 29. D.R. Merrit, F. Weinhaus, The pressure curve for a rubber balloon. *Am. J. Phys.* ***46***, 976-977 (1978).
328 30. E. Verron, R.E. Khayat, A. Derdouri, B Peseux, Dynamic inflation of hyperelastic spherical
329 membranes. *J. Rheol.* ***43***, 1083-1097 (1999).
330 31. K.-N. Tu, A.M. Gusak, "Appendix A: Laplace Pressure in Nonspherical Nanoparticle" in *Kinetics in*
331 *Nanoscale Materials* (Wiley, New Jersey, ed. 2, 2014), pp. 280-281.
332 32. J. Hu, S. Chen, W. Hu, S. Lü, M. Long, Mechanical point loading induces cortex stiffening and actin
333 reorganization. *Biophys. J.* ***117***, 1405-1418 (2019).
334 33. D.J. Acherson, *Elementary Fluid Dynamics* (Clarendon Press, Oxford, 1990).
335 34. L.-A. Lamiré, et al, Gradient in cytoplasmic pressure in the germline cells controls overlying
336 epithelial cell morphogenesis. biorxiv doi.org/10.1101/440438 (2020).
337 35. H.O. Gutzeit, The role of microfilaments in cytoplasmic streaming in *Drosophila* follicles. *J. Cell Sci.*
338 ***80***, 159-169 (1986).
339 36. M, Krieg et al., Tensile forces govern germ-layer organization in zebrafish. *Nat. Cell Biol.* ***10***, 429-
340 436.
341 37. R.E. Karess, et al., The regulatory light chain of nonmuscle myosin is encoded by spaghetti-squash, a
342 gene required for cytokinesis in *Drosophila*. *Cell* ***65***, 1177-1189 (1991).
343 38. C.G. Vasquez, M. Tworoger, A.C. Martin, Dynamic myosin phosphorylation regulates contractile
344 pulses and tissue integrity during epithelial morphogenesis. *J. Cell Biol.* ***206***, 435-450 (2014).
345 39. W.M. Bement et al., Activator-inhibitor coupling between Rho signaling and actin assembly makes
346 the cell cortex an excitable medium. *Nat. Cell Biol.* ***17***, 1471-1483 (2015).
347 40. F.M. Mason, S. Xie, C.G. Vasquez, M. Tworoger, A.C. Martin, RhoA GTPase inhibition organizes
348 contraction during epithelial morphogenesis. *J. Cell Biol.* ***214***, 603-617 (2016).
349 41. J.B. Michaux, F.B. Robin, W.M. McFadden, E.M. Munro, Excitable RhoA dynamics drive pulsed
350 contractions in the early *C. elegans* embryo. *J. Cell. Biol.* ***217***, 4230-4252 (2018).

351 42. J.L. Bos, H. Rehmann, A. Wittinghofer, GEFs and GAPs: critical elements in the control of small G
352 proteins. *Cell* ***129***, 865-877 (2007).
353 43. D.R. Cook, K.L. Rossman, C.J. Der, Rho guanine nucleotide exchange factors: regulators of Rho
354 GTPase activity in development and disease. *Oncogene* ***33***, 4021-4035 (2014).
355 44. K. Kimura, et al., Regulation of myosin phosphatase by Rho and Rho-associated kinase (Rho-kinase).
356 *Science* ***273***, 245-248 (1996).
357 45. C.G. Winter, et al., *Drosophila* Rho-associated kinase (Drok) links Frizzled-mediated planar cell
358 polarity signaling to the actin cytoskeleton. *Cell* ***105***, 81-91 (2001).
359 46. M. Amano, et al., Phosphorylation and activation of myosin by Rho-associated kinase (Rho-kinase).
360 *J. Biol. Chem.* ***271***, 20246-20249 (1996).
361 47. M. Sebbagh, et al., Caspase-3-mediated cleavage of ROCK I induces MLC phosphorylation and
362 apoptotic membrane blebbing. *Nat. Cell Biol.* ***3***, 346-352 (2001).
363 48. K. Miura, et al., ARAP1: a point of convergence for Arf and Rho signaling. *Mol. Cell.* ***9***, 109-19
364 (2002).
365 49. S. Huelsmann, J. Ylänne, N. H. Brown. Filopodia-like actin cables position nuclei in association with
366 perinuclear actin in *Drosophila* nurse cells. *Dev. Cell* ***26***, 604–615 (2013).
367 50. L.C. Wong, P. Schedl. Dissection of *Drosophila* ovaries. *J. Vis. Exp.* ***1***, 52 (2007).
368 51. M. Prasad, A. C. Jang, M. Starz-Gaiano, M. Melani, D. J. Montell. A protocol for culturing
369 *Drosophila melanogaster* stage 9 egg chambers for live imaging. *Nat. Protoc.* ***2***, 2467-2473 (2007).
370 52. L.A. Perkins, et al. The transgenic RNAi project at Harvard Medical School: resources and validation.
371 *Genetics* ***201***, 843-852 (2015).

372 **Figures 1 to 4**

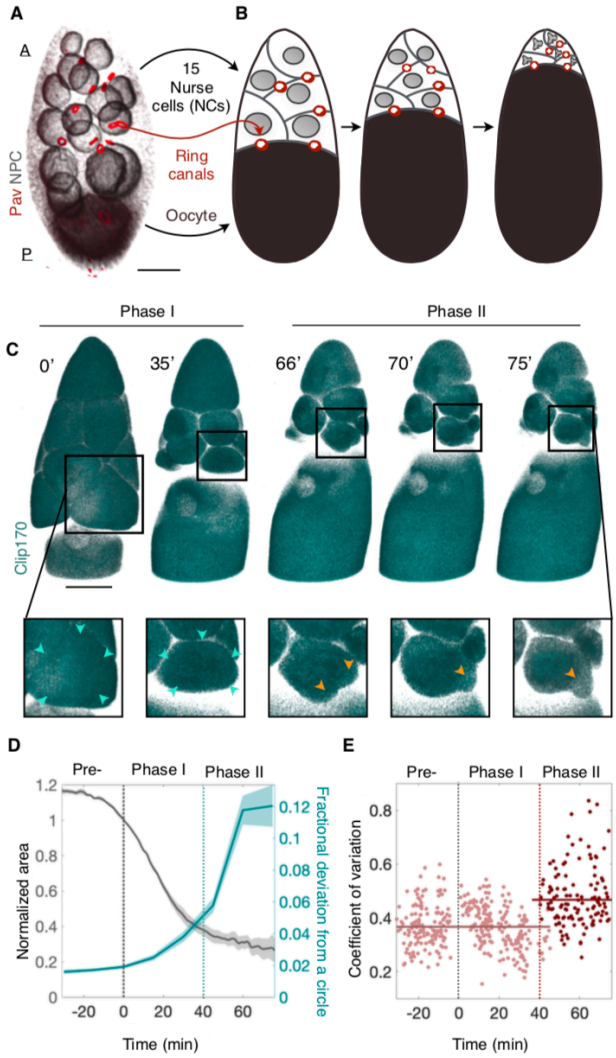

373

374 **Fig. 1. Nurse cell (NC) dumping unfolds in two phases**. **A**. 3D-rendered confocal image of an egg
375 chamber comprising 15 anterior (A) NCs (*Nuclear pore complex, NPC*; gray) and one posterior (P)
376 oocyte (black) connected through ring canals (*Pavarotti, Pav*; red). **B**. Schematic illustration of NC
377 dumping: NCs shrink as their cytoplasm flows into the oocyte through ring canals (Fig. S1A). **C**. 3D-
378 rendered time-lapse confocal images of an egg chamber expressing *Clip170::GFP* undergoing NC
379 dumping. Blowups show a nurse cell first shrinking uniformly (cyan arrowheads; Phase I) before
380 undergoing spatially nonuniform shape deformations and bleb-like protrusions (yellow arrowheads; Phase
381 II) that imply increased actomyosin contractility. Scale bar in **A** and **C** = 40 μm. **D**. Quantification of

382 changes in cell size (gray) and changes cell shape (i.e. fractional deviation from a circle; Fig. S2, C and
383 D) prior to NC dumping (Pre-), and during Phases I and II. Onset of non-uniform deformations (dashed
384 cyan line) occurs ~40 minutes into NC dumping for the samples analyzed ($N = 4$). **E**. Coefficient of
385 variation of cortical Sqh intensity during 'NC dumping', showing a transition (dashed red line) from
386 uniform ($N = 412$; Phase I) to non-uniform ($N = 122$; Phase II) distribution at ~40 minutes into NC
387 dumping, concomitant with onset of dynamic cell shape deformations.

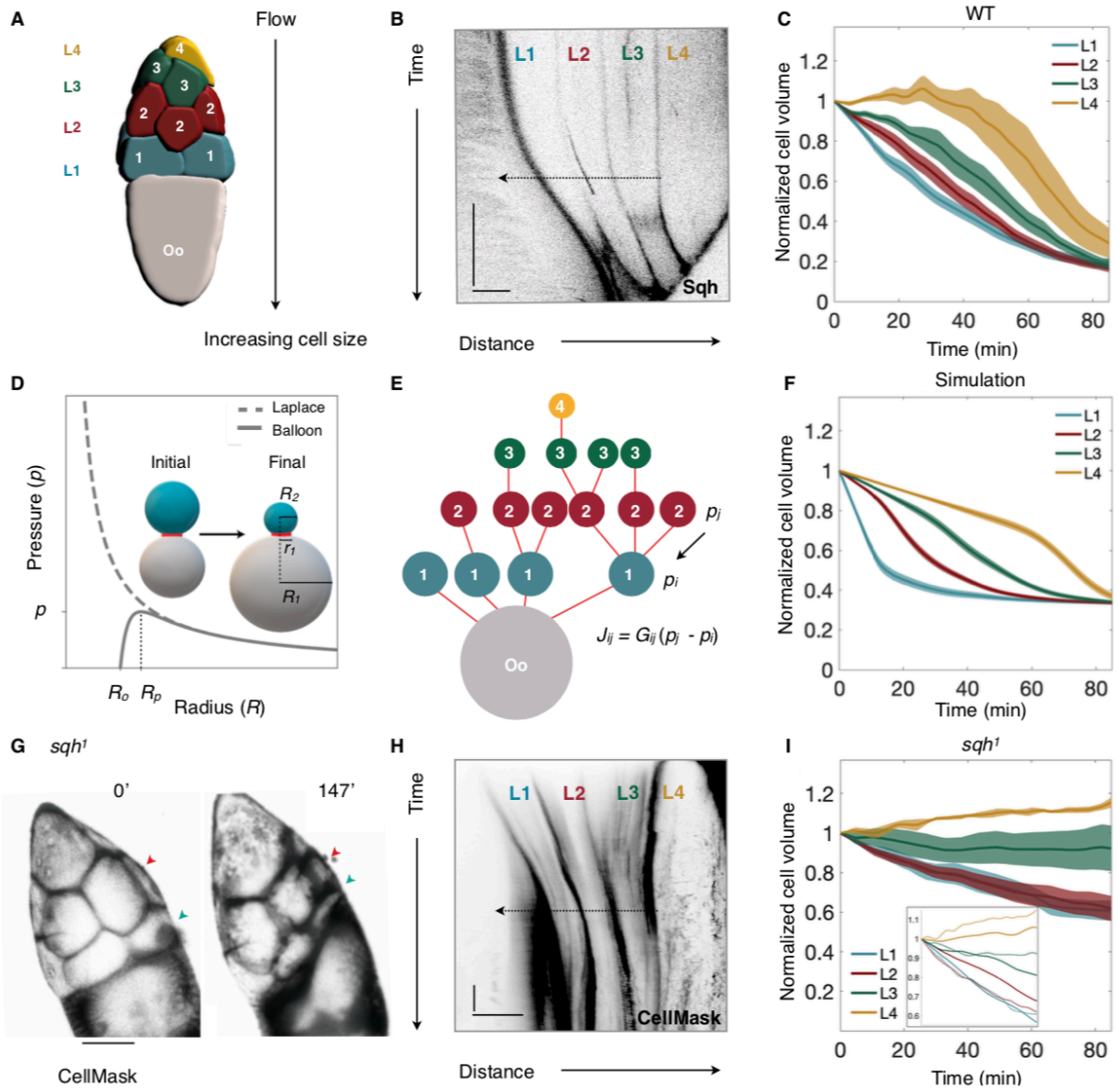

Fig. 2. A pressure-driven networked-flow model explains dynamics of NC dumping. **A**. 3D-reconstruction of a germline cyst showing the NCs' arrangement into four layers relative to the oocyte (Oo). During NC dumping, cytoplasm flows in direction of increasing cell size. **B**. Kymograph of Sqh intensity in WT, illustrating hierarchical onset of NC dumping across the 4 NC layers (L1-L4); arrow indicates direction of flow. Scale bars = 30 min, 50 μm; black indicates highest intensity. **C**. Plot of normalized NC volumes (V/V_o) during NC dumping for each layer from live imaging; $t = 0$ is onset of NC dumping; solid line indicates average; envelopes show standard error (N = 15, 12, 9, 5 cells for layers 1, 2, 3, and 4, respectively). **D**. Plots of Young-Laplace's law and the corrected pressure law for elastic

397 balloons. Pressure is at its maximum, p_{max}, at radius R_p; R_o is the uninflated balloon radius; r_{12} is the radius
398 of the pipe connecting balloons 1 and 2. Schematic illustrates the two-balloon problem, where the smaller
399 balloon (cyan) empties into the larger balloon (gray). **E**. Network representation of the germline cyst in **A**
400 showing cells' relative sizes and connections; cells are shown as nodes and ring canals as edges. **F**. Plot of
401 normalized NC volumes from simulations of fluid flow in the germline cyst using the best fit parameter
402 set (solid line); envelopes show standard error constructed from the ten nearest sets in parameter space (N
403 = 11). Time is scaled by the physical constants of the model. **G**. *sqh*^{1} germline mutant showing NCs in the
404 first (blue arrowhead) and second (red arrowhead) layers emptying into the oocyte. **H**. Kymograph of
405 CellMask intensity in *sqh*^{1} mutants, showing cytoplasmic transport from the first two layers. Scale bars =
406 30 min; 70 μm. **I**. Plot as in **C** of normalized NC volumes over time in *sqh*^{1} germline clones; (N = 14, 17,
407 7, 6 cells for layers 1, 2, 3, and 4, respectively); inset shows WT cell volume trajectories from **C** (solid
408 lines), re-scaled in time and overlaid with *sqh*^{1} mutant data (dashed lines), demonstrating slower yet
409 hierarchical cytoplasmic transport.

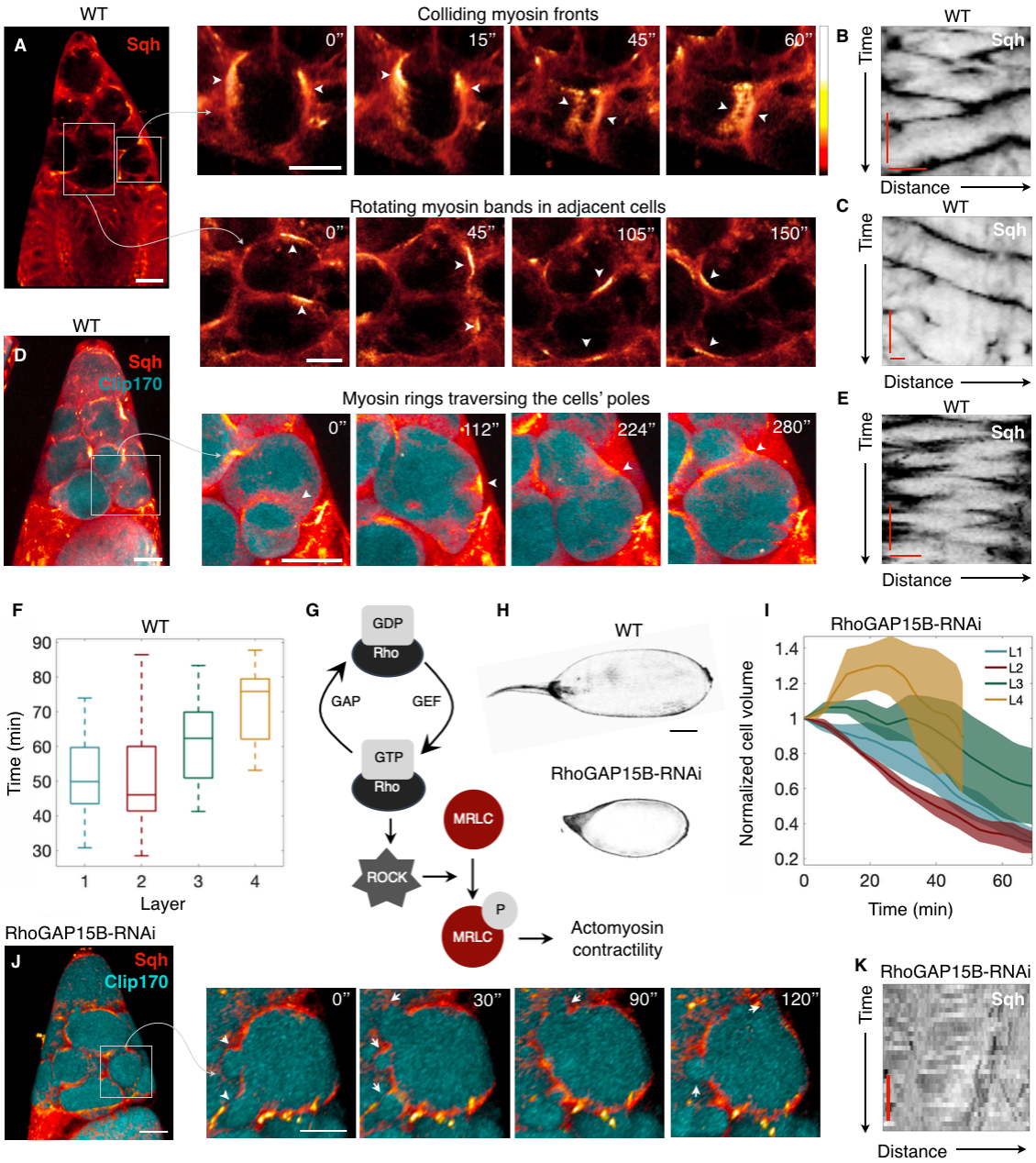

Fig. 3. NC dumping completion requires Rho-regulated wave-like actomyosin dynamics. A. Heat map of an egg chamber expressing *sqh::mCH*; blowups show NCs with dynamic actomyosin cortical waves as colliding fronts (top) and rotating bands (bottom) in adjacent NCs, with respective kymographs of Sqh intensity around NCs’ perimeter (**B**, **C**). **D**. Heat map of an egg chamber expressing *sqh::mCH* and *Clip170::GFP* (cyan); blowups show a NC with an actomyosin ring (arrowhead) traversing the cell’s opposing poles and deforming cell shape, with kymograph of Sqh intensity in **E**. **F**. Box-and-whisker plot

417 of median time at which nonuniform and persistent cell deformations are first observed following onset of
418 NC dumping in each layer (center line = median; edges = upper and lower quartiles; whiskers extend to
419 extrema; $N = 20, 22, 16, 5$ cells for layers 1, 2, 3, and 4). **G**. The Rho/ROCK signaling pathway regulates
420 phosphorylation of the myosin regulatory light chain (MRLC) and actomyosin contractility. **H**.
421 Comparison between wild-type (WT; top) and RhoGAP15B-depleted (bottom) egg chambers. Scale bar =
422 50 μm. **I**. Plot of normalized NC volumes during NC dumping for each layer from live imaging of
423 RhoGAP15B knockdowns; $t = 0$ is onset of NC dumping; solid line indicates average; envelopes show
424 standard error ($N = 7, 6, 3, 2$ cells for layers 1, 2, 3, and 4, respectively). The trajectory for the L4 cells
425 stops at $t \sim 50$ minutes due to membrane breakdown (*Methods*). **J**. RhoGAP15B-depleted germline
426 expressing *sqh::mCH* and *Clip170::GFP;* blowup shows smaller short-lived cell protrusions as opposed
427 to the cell-scale dynamic deformations observed in WT. **K**. Kymograph of Sqh intensity along the
428 perimeter of a cell in a RhoGAP15B knockdown at a comparable time to **B**, **C**, and **E**, illustrating
429 disrupted wave dynamics; black indicates highest intensity. The time scale bar is 5 minutes, while the
430 horizontal axis represents fractional distance along cell perimeter. Scale bar in **A**, **D**, and **J** = 40 μm; scale
431 bar in blowups = 20 μm; kymograph scale bars in **B**, **C**, and **E** = 5 min; 10 μm.

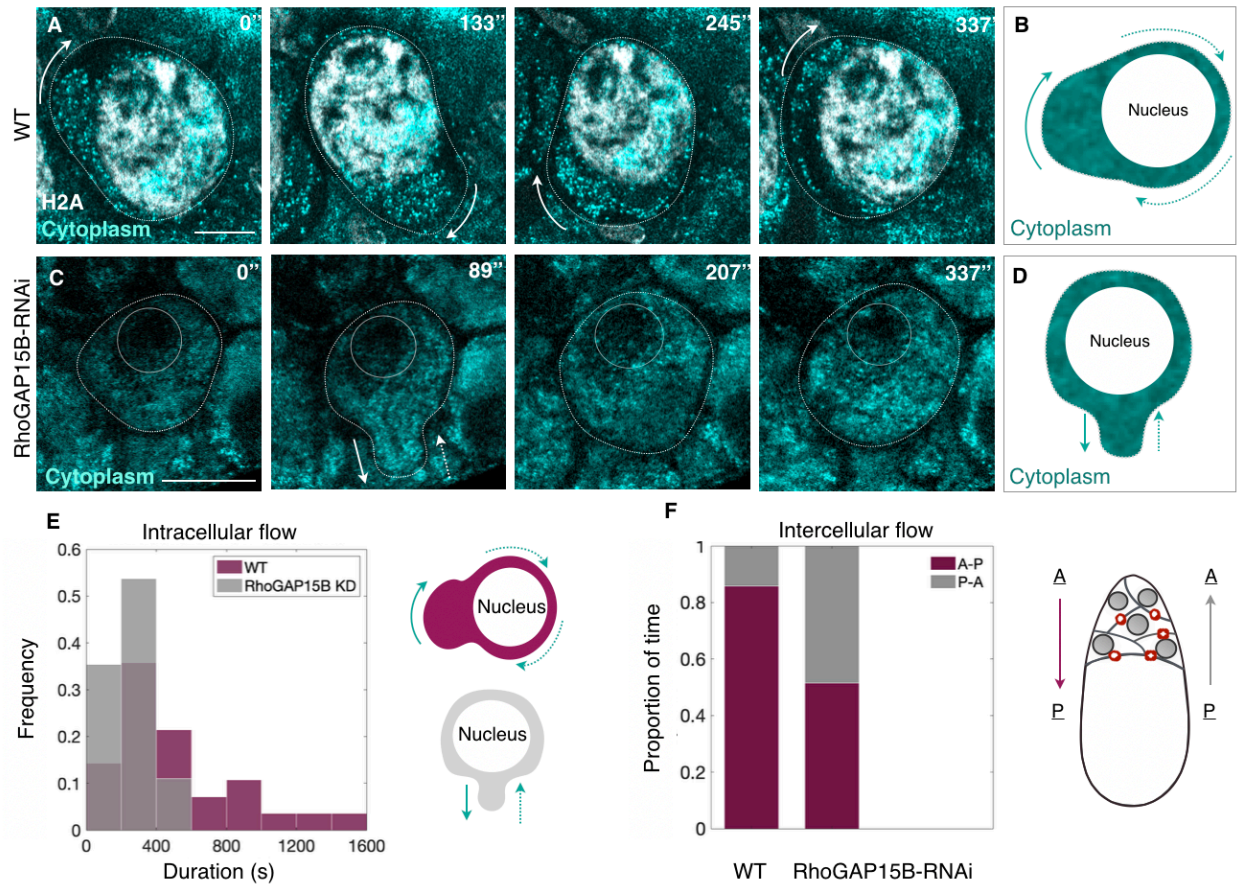

Fig. 4. Actomyosin contractions enable continuous intercellular flow in shrunken NCs. A. Time-lapse images from reflection-mode microscopy showing cytoplasm (cyan) flowing around a NC nucleus (H2A, white) as persistent actomyosin waves deform cell shape. **B**. Illustration of cytoplasmic flow observed in **A**, where arrows point in the direction of flow. **C**. Erratic and short-lived cytoplasmic flow in a germline RhoGAP15B knockdown, illustrated in **D**, highlighting the lack of repeated revolutionary motions observed in WT. Scale bars in **A** and **C** = 20 μm. **E**. Histogram of the duration of observed intracellular cytoplasmic flow events in WT and RhoGAP15B knockdowns (WT: $N = 28$ events; RhoGAP15B-RNAi: $N = 82$). **F**. Bar plot of the proportion of time anterior-to-posterior (A-P) versus posterior-to-anterior (P-A) flows were observed through ring canals in WT and in RhoGAP15B-RNAi egg chambers (WT: 6 events of intercellular flow spanning 30 minutes total; RhoGAP15B knockdowns: 29 events spanning 54 minutes).

Supplementary Information for

Dynamics of hydraulic and contractile wave-mediated fluid transport during *Drosophila* oogenesis

Authors

Jasmin Imran Alsous, Nicolas Romeo, Jonathan A. Jackson, Frank Mason, Jörn Dunkel, Adam C. Martin

Corresponding authors

Adam C. Martin (acmartin@mit.edu)

Jörn Dunkel (dunkel@mit.edu)

This PDF file includes:

Materials and methods

Figures S1 to S8

Tables S1 to S3

Legends for Movies S1 to S10

References

Other supplementary materials for this manuscript include the following:

Movies S1 to S10

Materials and Methods

Image Analysis. We used FIJI (1) and Bitplane's Imaris (2) to analyze our images and movies, and Matlab (3) for aligning data and generating plots. Measurements and sample sizes are recorded in Table S2.

Measurements of cell sizes, volume estimates, and creation of cell volume time courses. Nurse cells are large cells (~50-70 μm in diameter at onset of NC dumping) and often move noticeably in all three dimensions during NC dumping. As a result, we were unable to consistently capture the entire germline cyst during live imaging, preventing us from obtaining complete cell volume measurements. Instead, we used area measurements as a proxy for volume measurements, assuming cells are roughly spherical and that the volume of a cell could be calculated from its midplane area as $V = \frac{4}{3\sqrt{\pi}} A^{3/2}$. After normalizing to initial sizes, this allowed estimation of normalized volumes as $\frac{V}{V_0} = \left(\frac{A}{A_0}\right)^{3/2}$, where A_0 and V_0 are the area and estimated volume at the beginning of dumping for that cell. Areas were measured in FIJI by manually outlining each cell in the *z*-plane of largest cross-section at roughly 5-minute time intervals over the usable course of the movie. We confirmed that area measurements are a good proxy for cell volume by comparing the result of raising our normalized area measurements to the 3/2 power with the few usable normalized volume measurements acquired using Imaris (Fig. S1, B to D).

Nurse cells were not included in the analysis if any of the following occurred before enough data could be taken to generate a trajectory for changes in cell volume during NC dumping: the cell was positioned in *z* such that its cross-sectional area did not show a maximum within the imaged depth, the cell fused with a neighbor early in the acquired time course, or the cell shape was significantly deformed from a sphere when viewed in 3D. Times taken from microscopy metadata were shifted either to align all traces by the time of their dumping onset or to align by wave/deformation onset; that is, to make $t = 0$ correspond to the first frame at which the behavior in question was observed. Because the time required to complete a *z*-stack varied between movies, calculation of mean time courses of normalized volume estimates required temporal alignment. Volume time courses were aligned in Matlab through linear interpolation to 1-minute time intervals. For calculations of layer averages, individual time courses were then truncated to times at which data was collected for all cells to prevent discontinuities in the mean time course resulting from a variable number of measurements. For mean time courses of all cells together, a larger time range was included, and means were produced by grouping data into 20-minute bins and plotting bin averages. Time courses of NC cluster and oocyte lengths (Fig. S1A) were generated using the same methods as for layer

31 averages but using normalized length measurements of the NC cluster and oocyte along the long axis of
32 the egg chamber instead of areas. For the NC cluster and oocyte length time courses, $N = 4$ egg chambers
33 for $t = -28$ to 130 minutes and $N = 3$ egg chambers at other times.
34
35 **Dumping onset kymographs and plots.** Using maximum intensity projections (MIPs) through z, a linear
36 region of interest (ROI) was drawn across the long axis of egg chambers using FIJI, and the
37 MultipleKymograph plugin was used to generate kymographs of myosin (*sqh::GFP* or *sqh::mCH*) or
38 membrane (*Ecad::GFP* or *Gap::mCH*) intensity over time along the line. To generate a plot of average
39 dumping onset rate and progression, several such kymographs were generated, the front between
40 centripetal follicle cells and the NC cluster (i.e. the posterior boundary of the NC cluster) was outlined
41 manually on the kymograph, and its coordinates were taken from FIJI. Coordinates of the fronts were
42 input to Matlab and aligned by subtracting the baseline (initial position of the front). Linear measurements
43 of the posterior NC cluster boundary location showed an S-shaped curve with a clear inflection point, so
44 interpolation was performed as described above and times were shifted to align the inflection in each time
45 course in order to avoid ambiguities in determining dumping onset by eye.
46
47 **Time measurements of wave onset.** Dumping and wave onset times were collected by viewing movies
48 in FIJI. Time differences between dumping and wave onset were determined, cells were grouped by layer,
49 and layer statistics were calculated using Microsoft Excel.
50
51 **Analysis of actomyosin levels**. Mean and standard deviation of fluorescence intensity along a segment of
52 the cell perimeter were measured for different time points for germline cysts labeled with either
53 *sqh::mCH* or *sqh::GFP*. Segments were chosen to avoid tricellular junctions, where Sqh intensity was
54 typically much higher than surrounding regions. In addition, the top and bottom 2-3 slices were excluded
55 from the analysis and the outer curves of the nurse cells were avoided to prevent myosin variation in the
56 surrounding follicle cells from affecting the measurements. Note that the ellipsoidal shape of the germline
57 cysts resulted in changes in intensity solely from the amount of tissue between the objective and the
58 optical section; unlike for a flat tissue, this intensity decrease was not consistent across a plane. As a
59 result, segments of the cell perimeter were limited in length and confined to regions without a noticeable
60 intensity gradient along the ROI. Lastly, since a measurement of intensity alone would not differentiate
61 between actual relative biological changes in myosin levels/distribution and imaging artifacts, the
62 coefficient of variation (COV), defined as the ratio of standard deviation to mean (σ/μ), was calculated
63 for each measurement to determine the fractional variability in intensity along the membrane and allow
64 comparison between different cells and germline cysts (Fig. 1E; Fig. S3B). As a control, the same process

was repeated for cells labeled with *Resille::GFP*, a membrane marker (Fig. S3C). Measurements were grouped into three phases, the first corresponding to times prior to wave onset, the second to times at which the membrane showed only uniform shrinkage maintaining cell shape, and the third to times at which the membrane deformed heavily and non-uniformly, changing cell shape. Average values of the COV for each group were calculated by weighting each measured COV by the length of the corresponding ROI. Two-tailed Welch's *t* tests were performed using Matlab's ttest2 function with the 'unequal variance' option.

Generation of actomyosin kymographs. For wildtype (WT) wave behavior kymographs, ROIs were drawn on MIP time-lapse images along a curved path following the wave fronts (colliding waves), along the cell perimeter (rotating waves), or across the cell diameter (traveling rings), and wave kymographs showing Sqh levels were generated using FIJI as described above. MIPs through *z* were created using built-in FIJI tools. Cells used for actin behavior kymographs and the RhoGAP15B RNAi myosin kymograph moved significantly over the time period of interest, so ROIs were drawn around the perimeter of MIP time-lapse images, starting at the same location of the cell in each frame. Intensities around these perimeters were measured in FIJI, input to Matlab, aligned and scaled to their fractional position along the cell perimeter, and displayed as kymographs. The RhoGAP15B RNAi kymograph in Fig. 3K is of a layer 4 cell sufficiently long after dumping onset that a WT cell would have begun non-uniform contractions.

Quantification of cell deformation. Cell outlines were manually drawn in FIJI over MIPs of a cytoplasmic marker (*Clip170::GFP*) or a membrane marker (*Resille::GFP*); their coordinates were taken and input to Matlab, where the cell centroid and projected area were calculated and used to create a circular outline with the same centroid and area as the cell. At each time point, deviations of the measured outline from the circle were then calculated at 180 evenly-spaced angles from the centroid and normalized by the effective cell radius $r_{eff,t} = \sqrt{A_t/\pi}$ (Fig. S2): for a given angle θ_n at which the projected cell outline is a distance $r_{n,t}$ from the centroid, we defined fractional deformation as $\alpha_{n,t} = \frac{r_{n,t} - r_{eff,t}}{r_{eff,t}}$. To account for non-circular shapes of cells, which could change over time solely due to volume decrease, the magnitude of change in deformation profile from one time point to the next was then calculated and the root-mean-square (rms) value taken:

$$(\Delta\alpha_{rms})_t = \sqrt{\frac{1}{N}\sum_{n=1}^{N}\left(\alpha_{n,t} - \alpha_{n,(t-1)}\right)^2} \qquad (1)$$

where n indexes the angle and t the time point; $N = 180$ here. Measurements were aligned in time as described above, so time spacing between elements of α was the same for each cell.

Reflection-mode microscopy flow behaviors. For flow behavior quantification, types of flow were broken into two main categories: intercellular flow (through ring canals) and intracellular flow (induced within a cell by actomyosin waves). For intercellular flow, the direction could be further categorized as either anterior-to-posterior or posterior-to-anterior; the latter is the opposite of that required for complete 'NC dumping'. For each movie of WT or RhoGAP15B-depleted germline cysts, the duration of each type of flow behavior was recorded. For WT, there were 6 events of intercellular flow spanning 30 minutes total; for RhoGAP15B knockdowns, there were 29 events spanning 54 minutes. There were 28 intracellular flow events in WT for a total of 239 minutes, and 82 intracellular events spanning 338 minutes in RhoGAP15B knockdowns. Fig. 4E represents the actual duration of intracellular events, while the fraction of time undergoing each intercellular behavior was calculated and used to generate Fig. 4F.

Ring canal growth kinetics measurements. *Z*-stacks of egg chambers dissected at various stages (2 through 11) were acquired as described above. Inner ring canal diameter was measured using Imaris or Zen for every fully visible, undeformed ring canal (26 egg chambers, 10-15 ring canals per chamber, 370 canals total). The stage of oogenesis was estimated using morphological and size features (4) and converted to developmental time (5). Errors in matching measurements of ring canal diameters to a developmental stage within oogenesis arise from inherent variability in developmental rates and uncertainties in determining the exact age of the egg chamber as staging is based on morphological and size features.

3. Theory

Model. We modeled hydrodynamic flow on the stereotypical 16-cell tree that is the *Drosophila*'s germline cyst. Cells i and j are connected by ring canals, each of which can be approximated as a small cylindrical pipe of radius r_{ij} and length L. The viscosity of cytoplasm in *Drosophila* has been estimated *in vivo* (6) as $\mu \simeq 1\ Pa \cdot s$. At low Reynolds numbers ($Re = \frac{\rho_o U a}{\mu} \approx \frac{10^3\ kg}{m^3} \times \frac{10^{-6}\ m}{s} \times \frac{10^{-6}\ m}{1\ Pa{\cdot}s} = 10^{-9} \ll 10^{-3}$, with U a characteristic speed, a a length scale and ρ_o the density of the cytoplasm), flow through the ring canals is assumed to be incompressible Poiseuille flow. In this case, flow J_{ij} from cell j to i is

proportional to the difference in their respective pressures $(p_j - p_i)$, with the proportionality constant given by the hydraulic conductance G_{ij}.

The change in the volume of cell i is then determined by the total fluxes in and out of the cell:

$$\frac{dV_i}{dt} = \sum_{\langle i,j \rangle} J_{ij} = \sum_{\langle i,j \rangle} G_{ij}(p_j - p_i) \tag{2}$$

Here, the sum runs over the set of cells j connected to cell i by ring canals. Summing over all the cells, one can verify that the total cytoplasmic volume is conserved throughout the germline cyst, i.e. $\sum_i dV_i/dt = 0$ at all times.

Balloon pressure law. We model each cell i as a spherical 'balloon', with interior pressure p_i relative to the homogeneous pressure outside given by the modified Laplace pressure law (7):

$$p_i = \frac{2\gamma}{R_i}\left(1 - \left(\frac{R_{0,i}}{R_i}\right)^6\right) \tag{3}$$

Here, $R_i = 3V_i^{1/3}/4\pi$ is the radius of the i-th balloon, and γ is the surface tension of the shell, understood here as the generic energy cost to build an interface. As long as the cell is roughly spheroidal, the spherical approximation will not qualitatively alter the results.

To gain intuition about the behavior of this pressure law, consider two balloons (or two cells) that are connected by an open canal. There are two possible equilibrium configurations for which the pressure in both balloons is equal. In the first case, both balloons are of equal size and the system does not deviate from its initial configuration. In the second case, the balloons assume unequal sizes; that is, an initial size imbalance will be amplified until the pressures balance out. For instance, assuming that initially both balloon radii are larger than R_0, the initially larger balloon will grow to a radius $R_{large} \gg R_p$, whereas the other will shrink down to a radius $R_{small} < R_p$ where $R_p = 7^{1/6}R_0 \approx 1.38R_0$ is the radius at maximum pressure. Note that as R_i grows relative to the zero-pressure radius $R_{0,i}$, one recovers the usual Laplace pressure law, $p_i = 2\gamma/R_i$.

Alternative pressure laws. While the microscopic nature of a nurse cell is much more complex than a rubber balloon, cells can be considered effectively viscoelastic, with a filamentous cytoskeleton bearing

similarities to crosslinked semiflexible polymer networks such as rubber (8). Merritt and Weinhaus obtained the above pressure law for the case of an isothermal spherical rubber balloon, using a specific constitutive equation (also called *stress-strain equation*) (7), first derived by James and Guth for rubber in 1943 (9). In fact, as shown previously (10), one would obtain the same functional form for the pressure law for a neo-Hookean material, which itself is a particular case of a Mooney-Rivlin material for small enough extensions. Mooney-Rivlin materials are generally considered to be appropriate models of incompressible rubber-like materials and have been widely used to describe biological tissues, including the cellular cortex (11). If we were to relax the assumption of incompressibility, another family of constitutive relations would follow the Blatz-Ko model (10) and more complex variants. Since cells are usually considered more fluid-like than solid (12), the assumption of incompressibility is reasonable, rendering the Merritt and Weinhaus law an appropriate framework for this problem.

From a more physical viewpoint, to illustrate how a different microscopic model would provide a different power law correction to Young-Laplace's law, consider for instance a spherical shell of radius R consisting of particles that interact according to an repulsive short-range pair potential $V(x-y) = -g\delta^2(x-y)$. Assuming the particles' surface density is uniform $\rho(x) = \rho = N/(4\pi R^2)$, the energy contribution of this interaction is:

$$F = \frac{1}{2}\int d^2x d^2y\, \rho(x)\rho(y)V(x-y) = -\frac{g}{2}4\pi R^2\rho^2$$

In the presence of a surface tension, the differential of free energy would be, at constant temperature,

$$dF = -pdV + \gamma dA$$

where dA is the variation in area. The pressure as a function of radius would then be given by

$$p = -\frac{\partial F}{\partial V} + \gamma\frac{dA}{dV} = \frac{2\gamma}{R} - \frac{gN^2}{8\pi^2}\frac{1}{R^5} = \frac{2\gamma}{R}\left(1 - \left(\frac{R_0}{R}\right)^4\right)$$

with $2\gamma R_0^4 = gN^2/8\pi^2$. Here we see that the repulsive interaction potential ends up contributing a $1/R^n$ – a correction to Laplace's law.

Lastly, to test out whether different 'elastic' $1/R^n$ terms provide qualitative agreement with the data, we ran different simulations with varying values of n. While the slopes of curves varied, the directionality and layer-wise hierarchy of dumping order was preserved (Fig. S4B).

Hydraulic conductance. Nurse cells in the germline cyst are connected by ring canals. Assuming Poiseuille-type flow (13), the hydraulic conductance G of a cylinder of radius r and length L is given by:

$$G = \frac{\pi r^4}{8\mu L} \tag{4}$$

We use this formula to estimate the hydraulic conductance G_{ij} between cells i and j at the onset of NC dumping, adopting typical parameters $r \approx 5\ \mu m$ and $L \approx 2\ \mu m$ inferred from experimental imaging data.

To test whether such a surface tension-driven flow model could capture the observed dynamics of intercellular networked transport through ring canals, we first estimated the minimal effective surface tension required for Laplace pressure-driven flow at magnitudes comparable to those observed experimentally. The relative contributions of cortical tension versus in-plane membrane tension to cell surface tension are known to vary (14). Here, we combine both contributions into a single effective surface tension parameter γ that can be estimated from measurable quantities as described below:

$$\gamma = \frac{4\mu L R J}{\pi r^4} \tag{5}$$

To estimate an upper bound on J, the magnitude of flux through a single ring canal, we used the steepest rate of change in cell volume (Fig. 2C), multiplied it by the average volume of a layer 1 cell at NC dumping onset and obtained $J = 40\ \mu m^3/s$.

Using $\mu \simeq 1\ Pa \cdot s, L = 2\ \mu m, R \approx 30\ \mu m, J = 40\ \mu m^3/s, r = 5\ \mu m,$ we find a value of approximately $4 \cdot 10^{-3}$ mN/m for γ. This estimate for γ is at the lower end of literature reported values (15), consistent with the known fact that the nurse cell cluster have a relatively low basement membrane stiffness (16). We therefore contend that surface tension is sufficient for driving the observed transport dynamics.

In our subsequent calculations, we assumed that cell surface tension is constant in time for all cells as transport unfolds, which is supported by previous studies showing that plasma membrane tension is

actively regulated (e.g. through endocytosis) (17,18). We also assume first that cell surface tension is equal for all cells, justified by the fact that the cortical cytoskeletal network is invariant across cells within the germline cluster and does not appear to be significantly altered during the first phase of NC dumping, i.e., during the phase of surface tension-driven flow.

Additionally, to account for cell-to-cell variability in effective cell surface tension, we explored the effects of fluctuations of surface tension between cells in the model. To this end, we first adjusted the model to the experimental data, and subsequently allowed for approximately 10% surface tension fluctuations to account for variations in shape, basement membrane stiffness and other factors of cell-to-cell variability (see also Section '4. Simulations and optimization' below).

Dimensionless equations. Writing out equation (1) fully yields:

$$\frac{dV_i}{dt} = \sum_{\langle i,j \rangle} \frac{\pi\gamma r_{ij}^4}{4\mu L}\left[\frac{1}{R_j}\left(1-\left(\frac{R_{0,j}}{R_j}\right)^6\right) - \frac{1}{R_i}\left(1-\left(\frac{R_{0,i}}{R_i}\right)^6\right)\right] \tag{6}$$

To rewrite this equation in nondimensionalized form we define the characteristic time-scale $\tau_0 = 4\mu L/(\pi\gamma)$ and length scale ℓ_0 such that the initial oocyte volume is $100\ell_0^3 = 10^6\ \mu m^3$, yielding $\ell_0 \approx 20\ \mu m$. Using our estimate for γ from above, we find $\tau_0 \approx 0.6$ s. Defining the dimensionless radius $\hat{R}_i = R_i/\ell_0$, time $\hat{t} = t/\tau_0$, and volume $\hat{V}_i = V_i/\ell_0^3$, the dynamical equation takes the dimensionless form

$$\frac{d\hat{V}_i}{d\hat{t}} = \sum_{\langle i,j \rangle} \left(\frac{r_{ij}}{\ell_0}\right)^4 \left[\frac{1}{\hat{R}_j}\left(1-\left(\frac{\hat{R}_{0,j}}{\hat{R}_j}\right)^6\right) - \frac{1}{\hat{R}_i}\left(1-\left(\frac{\hat{R}_{0,i}}{\hat{R}_i}\right)^6\right)\right] \tag{7}$$

where the dimensionless pressure is given by $\hat{p}_i = \frac{1}{\hat{R}_i}\left(1-\left(\frac{\hat{R}_{0,i}}{\hat{R}_i}\right)^6\right)$.

Initial conditions and parameters. At $t = 0$, the sixteen cells have a well-characterized cell size pattern, as nurse cells further from the oocyte are smaller than those that are closer. The initial size distribution is determined as follows (19):

- the oocyte has a volume V_0 equal to the sum of all the nurse cells' volumes combined
- nurse cells at same distance $d = 1,2,3,4$ from the oocyte have the same cell volume V_d set by
- $\frac{V_{d+1}}{V_0} = \left(\frac{V_d}{V_0}\right)^\nu$ with $\nu \approx 0.84$.

Using these initial conditions, we computed the time-evolution of each cell's volume by numerically integrating the above set of ordinary differential equations. Our simulations (see section 4 below) showed that the trajectories strongly depend on the following parameters:

- Ring canal radii: Assuming that all ring canals at edge distance d from the oocyte have the same size r_d (Fig. S5A), we allow for variations of ring canals radii from their corresponding average experimental values by up to plus or minus 60% as described in the section 'Fitting procedure' below. Test simulations with equal ring canal sizes do not reproduce the experimentally observed dumping hierarchy.

- Zero-pressure radius: We assume all cells have a zero-pressure radius $R_{0,i} = \rho R_i(t = 0)$, where ρ is an adjustable parameter between 0 and 1.

Overall, this yields a total of five tunable parameters: the 4 ring canals sizes (r_1, r_2, r_3, r_4) and zero-pressure radius scale parameter ρ. A summary of the initial conditions and adjustable parameters is given in Table S3.

4. Simulations and Optimization

Implementation. The simulations were implemented in Python 3 augmented with the NumPy/SciPy libraries. The regular scipy.integrate.solve_ivp routine was used to solve the system of ordinary differential equations. Simulations were run until the system reached steady state. We have not conducted a full analysis of the stability of the fixed points in a more general setting. However, since our initial conditions are hierarchical, with the oocyte significantly larger than the next largest NCs, the dynamics most likely lie in the basin of attraction of the "1 large; 15 small" solution. Furthermore, those dynamics do not lead to perfectly empty balloons at steady state; indeed, as our experimental data show, completion of the dumping process requires active contractions, which are not included in the network flow model; we can therefore only reliably compare our simulation results with experimental data before the effects of myosin activity become too important, and the simulated steady-state has no physical relevance.

Fitting procedure. Experimental measurements provided us with the relative cross-sectional areas of cells, which we averaged per layer of cells at distance d from the oocyte. We then estimated the relative experimental volumes $V_d^{exp}(t)/V_d^{exp}(t=0) = \left(A_d^{exp}(t)/A_d^{exp}(t=0)\right)^{\frac{3}{2}}$, with time t expressed in units of τ_0. Our simulations then yield a set of volume trajectories $V_d^{sim}(t)$ for the average volume of cells in layer d.

Since the model developed here describes the first phase of NC dumping, namely, surface tension-driven flow, and does not include the effect of the actomyosin contractility, we compared our trajectories to experimental data taken before onset of actomyosin contractility only. Experiments show that this occurs when cells reach a characteristic fraction of their initial volume $V_{wave} = 0.25V(t=0)$ (Fig. S3). The sum of squares error between the experimental and simulation datapoints was then computed for each of the layer-averaged cross-sectional areas of cells, with a set of weights $g_d = (\frac{4}{15}, \frac{6}{15}, \frac{4}{15}, \frac{1}{15})$ such as $\sum_d g_d = 1$, reflecting the number of nurse cells in each layer. The error is then given by:

$$E = \sum_i \sum_{layers\ d=1}^{4} g_d \left(V_d^{exp} - V_d^{sim}\right)^2 (t_i) \tag{8}$$

This procedure was repeated as we searched through a grid of possible parameter values around their experimental averages, yielding the error plots shown in Fig. S4A (the final grid search was over 3.2

million simulations). The parameter sets that resulted in the smallest error are denoted as best fit parameters and recorded in Table S3.

Cell-to-cell variability. Once the parameters were determined through the method described above, we introduced fluctuations between individual cells in the effective surface tension. To that end, we sampled surface tension for each cell as $\gamma_i = \gamma_c(1 + \sigma\chi_i)$, where χ_i is a random variable sampled from the standard normal distribution with $\sigma = 0.1$. Results averaged over $N = 5{,}000$ trials are presented (Fig. S4C), where the envelope reflects one standard deviation of the fluctuation.

Ring canal fits. Measured ring canal diameters (Fig. S5A) were averaged for each layer and each stage. Exponential functions of the form $r(t) = r_o e^{t/\tau}$ were then fit to the averages using the 'fit' function in Matlab. The fit parameters are as follows: $r_o = 0.82, 0.55, 0.44$, and $0.67\ \mu$m and $\tau = 34.8, 31.2, 29.1$, and 38.0 hours for L1-L4, respectively. Values of R^2 are 0.93, 0.88, 0.85, and 0.83, respectively.

310 **Figures S1 to S8**

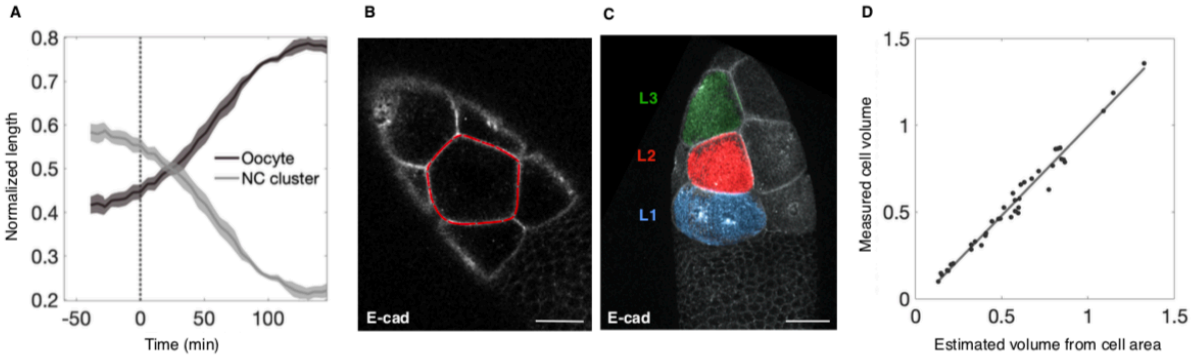

311
312

313 **Fig. S1. Verification of cell volume measurements. A**. Plot of fractional lengths of the NC cluster and
314 oocyte during NC dumping (N = 4 egg chambers). Line at t = 0 indicates onset of NC dumping. **B**.
315 Optical section of an egg chamber expressing *Ecad::GFP*, used to measure NC area as indicated by red
316 outline. **C**. 3D-rendered confocal image of an egg chamber expressing *Ecad::GFP* with surface
317 reconstructions of NCs for measuring NC volume. Scale bar in **B** and **C** = 40 μm. **D**. Plot of normalized
318 NC volume as measured from 3D Imaris surface reconstructions versus normalized NC volume estimated
319 from cell area measurements in FIJI, showing good agreement between both measurements; solid line
320 shows the best fit line; R^2 = 0.98, with slope = 1.03.

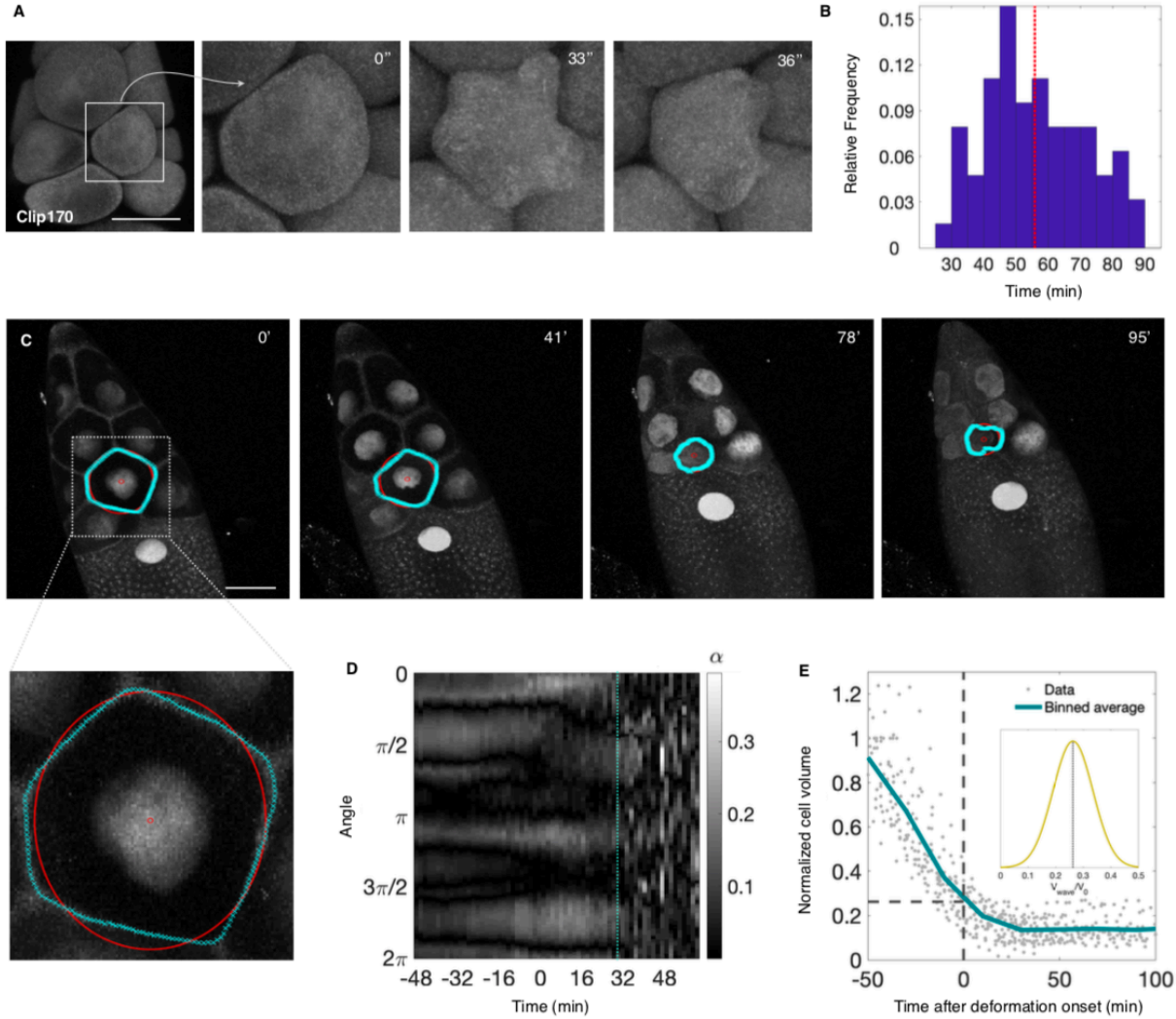

Fig. S2. Quantification of nurse cell shape deformations. A. 3D-rendered time-lapse confocal images of an egg chamber expressing *Clip170::GFP*; blowups show a cell contracting and deforming nonuniformly with onset of actomyosin waves. **B**. Histogram of time (min) following onset of NC dumping at which nonuniform NC deformations are first observed (red line shows average, $N = 63$ cells). **C**. Time-lapse maximum intensity projections (MIPs) of an egg chamber with labeled membranes (Resille) and nuclei (PCNA); outlined NC is analyzed in **D**. Blowup shows features used to quantify cell shape deformation: red dot indicates the cell's centroid; red outline indicates a circle with the same projected area as the NC; cyan outline shows point-wise cell shape. Scale bar in **A** and **C** = 40 μm. **D**. Kymograph of fractional deviation of NC shape from a circle, α, based on Resille, obtained from the MIP in **C**; line (cyan) marks beginning of nonuniform cell deformations. **E**. NC volume changes of different NCs ($N = 30$ cells) during NC dumping; $t = 0$ defines onset of nonuniform cell deformations. Inset shows the distribution of normalized cell volumes (V/V_o) at onset of cell deformations.

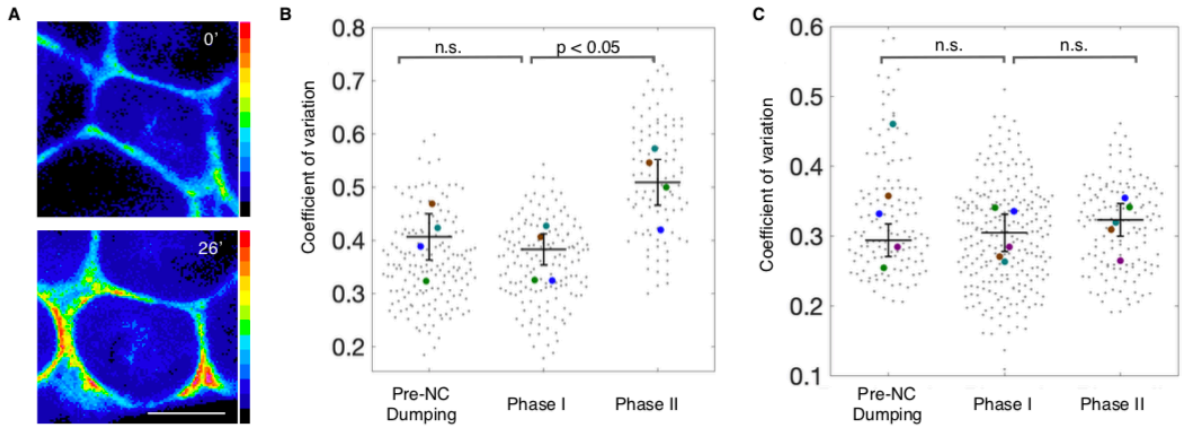

Fig. S3. Verification of Sqh distribution measurements. A. Heat map of Sqh intensity along the perimeter of an NC in an optical section during NC dumping, showing an increase in intensity and change in distribution. Scale bar = 20 μm. **B**. Swarm plot of the coefficient of variation of Sqh intensity along the cell perimeter in NCs prior to the onset of NC dumping (pre-NC dumping), and during Phases I and II of NC dumping, showing a statistically significant difference in Sqh distribution (p-value < 0.05) (N = 4 cells; 534 measurements). **C**. Swarm plot as in **B**. showing the coefficient of variation of Resille (a membrane marker) intensity at the cell perimeter in NCs, showing no statistically significant changes in its distribution prior to NC dumping, or between Phases I and II (p-value > 0.05; N = 5 cells; 504 measurements). Horizontal lines and error bars represent means and standard error, respectively; coloured dots represent mean of each NC.

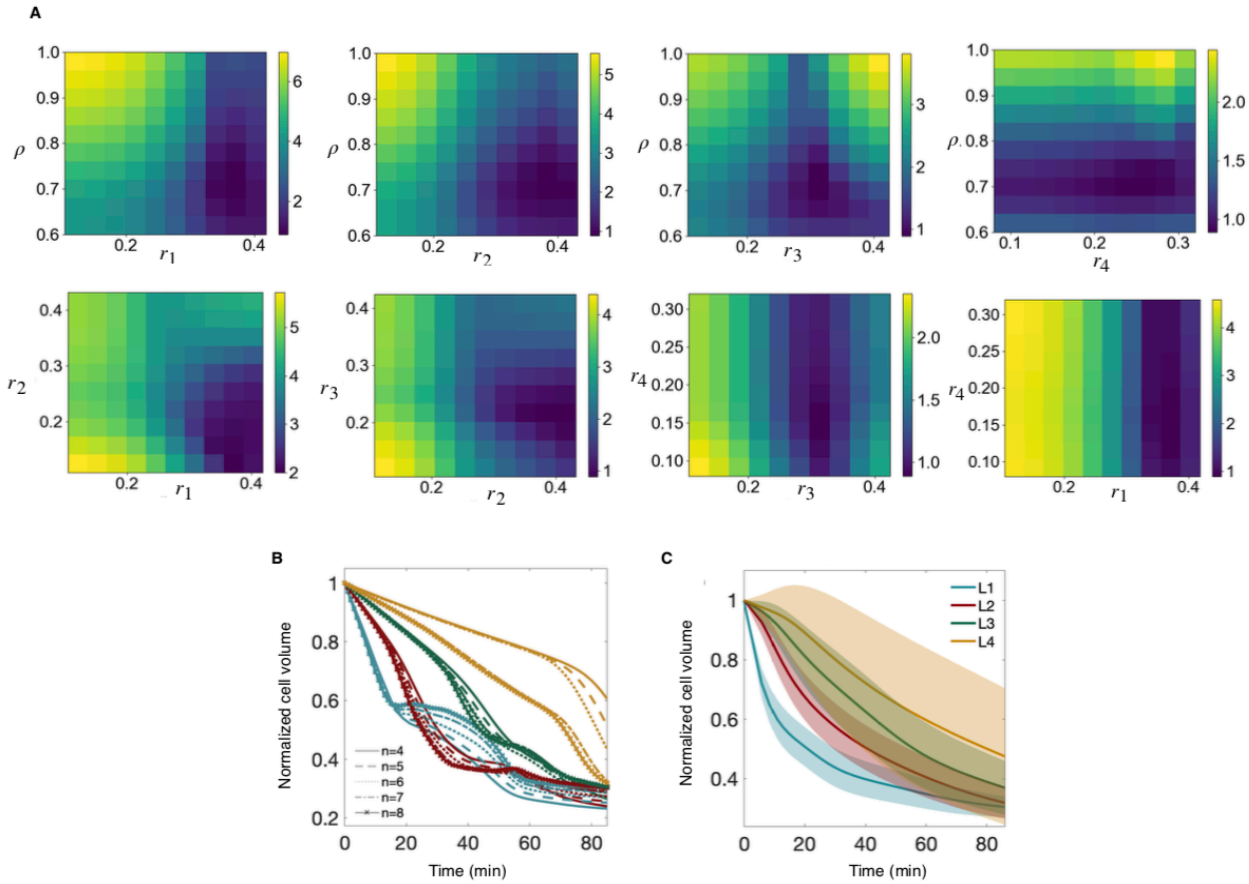

Fig. S4. Grid search through parameter space and input parameters of the model. A. Two-dimensional slices of the simulation error as defined in *Methods* measured on the 5-dimensional grid space spanned by the sampled parameter ranges (r_1, r_2, r_3, r_4, ρ). For a given pair of parameters, the remaining parameters are at their best-fit values. Colour bar refers to simulation error ($\sigma = 0.1$; see *Methods*). **B**. Results from simulations for varying values of n, the exponent in the correction term to the Young-Laplace law, showing that intercellular transport hierarchy and qualitative behaviors are maintained for the values of n tested. **C**. Results from simulations averaged over 5,000 trials, where surface tension of each cell is sampled from a normal distribution; envelope reflects half a standard deviation of the fluctuations. As seen in the envelope for L4, in several of these simulations the L4 cell increases in size due to backflow from its downstream L3 cell - a feature of NC dumping that has been reported in previous studies (20).

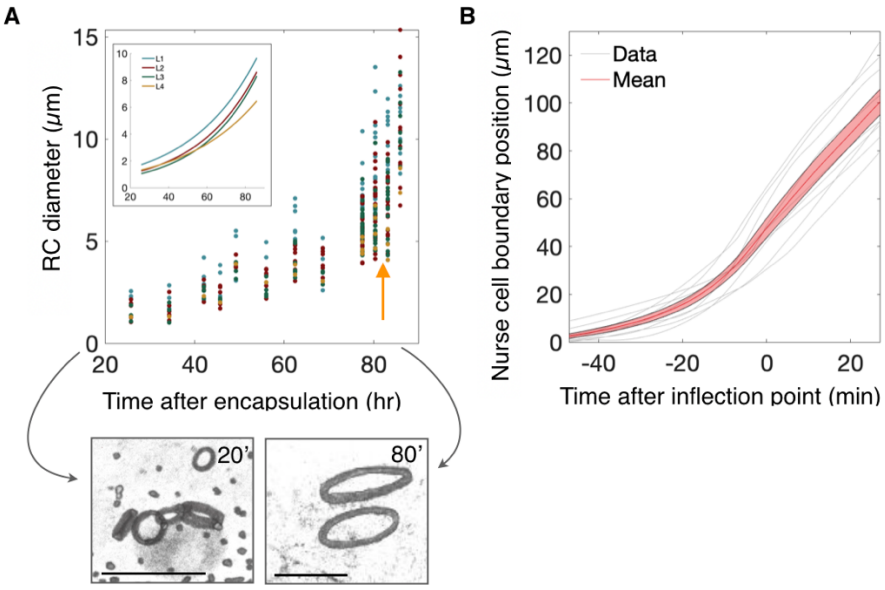

Fig. S5. Increase in effective ring canal size correlates with NC dumping onset. A. Increase in ring canal diameter during oogenesis, with rapid growth occurring prior to onset of NC dumping (arrow). Inset shows exponential fits to ring canal diameters of the form $d(t) = d_o e^{t/\tau}$ where $d_o = 0.78, 0.43, 0.36, 0.64\ \mu m$, $\tau = 34.8, 31.2, 29.1, 38$ hours; $R^2 = 0.93, 0.88, 0.85,\ 0.83$ for L1-L4, respectively. Layers are colored as in Figure 2. Arrows point to 3D-rendered confocal images of ring canals at ~20 and ~80 hours after encapsulation of the germline cyst (i.e. oogenesis Stage 1). Scale bar = 10 μm. **B**. Measurements of the position of the most-posterior edge of the NC cluster over time, where t = 0 is fastest rate of change in position of said edge. Cytoplasmic transport is thus accelerated during NC dumping (envelope shows standard error; N = 9 egg chambers).

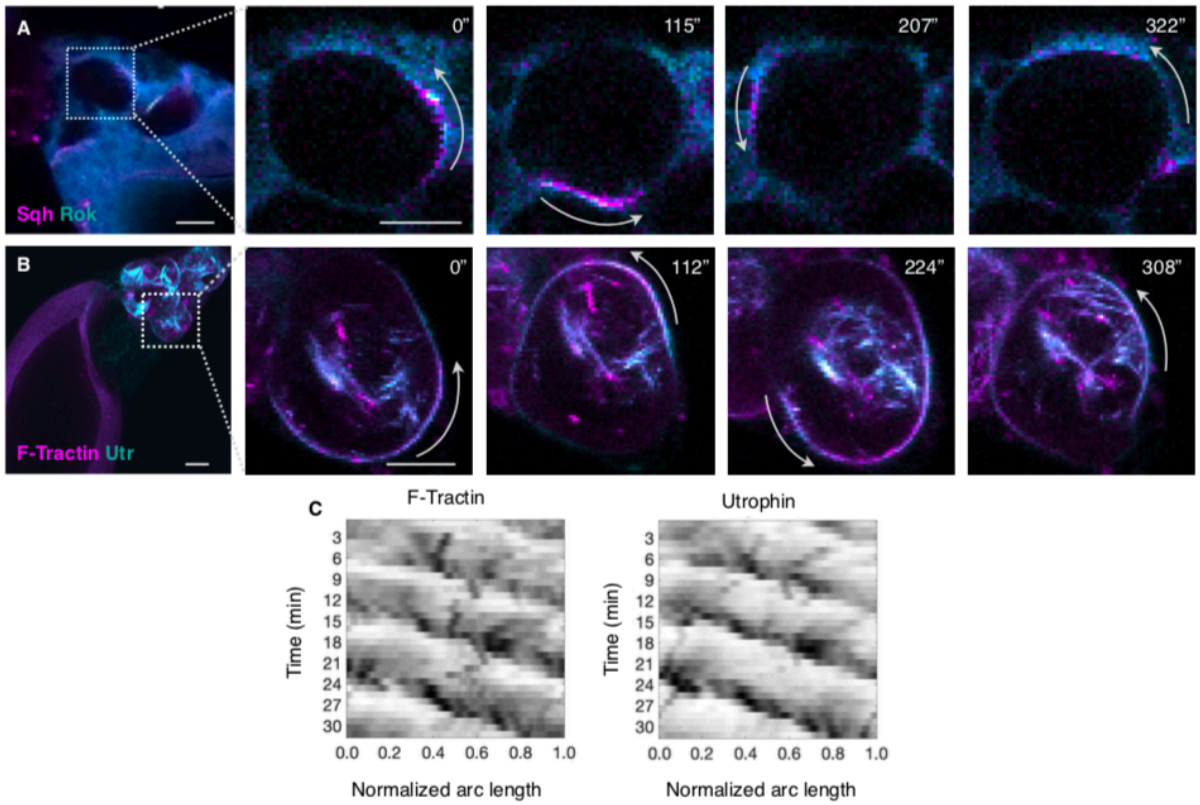

Fig. S6. Rho-regulated actomyosin wave dynamics during NC dumping. A. Egg chamber expressing *sqh::mCH* (magenta) and *ubi>GFP::rok* (cyan). Rok, upstream of Sqh, exhibits similar wave-like dynamics, seen in blowup as bands rotating along the NC cortex (arrows). **B**. Egg chamber expressing *F-tractin::TdTom* (magenta) and *Utr::GFP* (cyan), with blowup showing both actin-binding proteins exhibiting wave-like dynamics, with bands rotating along the cell cortex (arrow). Scale bars in **A** and **B** = 20 μm. **C**. Kymographs of F-tractin and Utrophin wave dynamics during actomyosin-mediated phase of NC dumping; black indicates highest intensity.

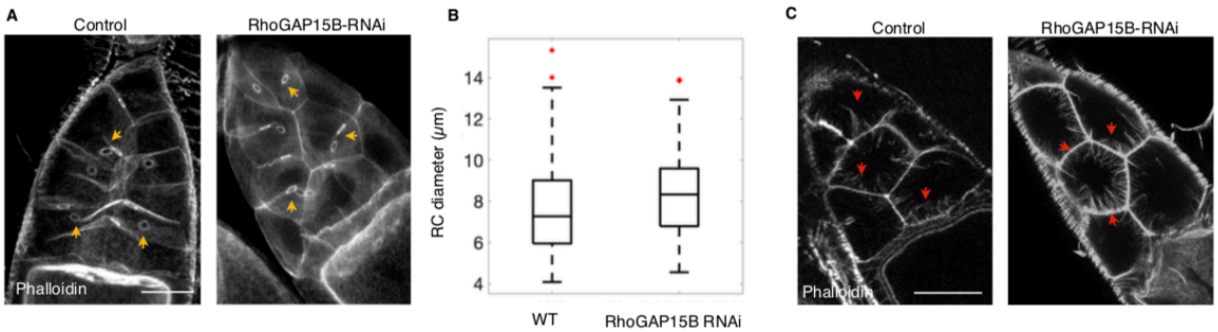

Fig. S7. Ring canals and actin cables in WT and RhoGAP15B-depleted egg chambers. A. 3D images of a control egg chamber (left) and an egg chamber with a RhoGAP15B-depleted germline cyst (right) stained with Phalloidin to show comparable ring canal structure to WT (arrows). **B**. Box plot of ring canal diameters (μm) in WT and in RhoGAP15B germline knockdowns (N = 162 ring canals for WT; 142 for RhoGAP15B-RNAi at oogenesis stage 10 and 11; red pluses mark data points > 1.5xIQR from median). **C**. Optical section of a control egg chamber (left) and an egg chamber with a RhoGAP15B-depleted germline (right) stained with Phalloidin; arrowheads point to actin cables that extend from the cell cortex to tether NC nuclei during NC dumping to prevent their occluding the ring canals. Scale bar in **A** and **C** = 40 μm.

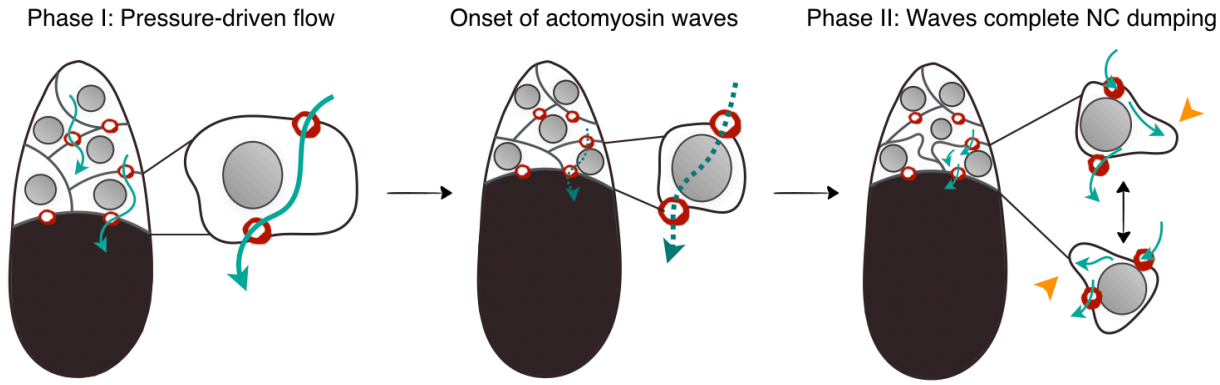

Fig. S8. Physical and biochemical mechanisms cooperate to enable NC dumping. Schematic of the proposed model for the contribution of pressure-driven flow with baseline cortical tension and actomyosin-dependent flows to directional and complete NC dumping. Arrows show direction of intercellular flow; dashed arrow indicates interrupted flow; arrowheads point to actomyosin-mediated cell deformations that permit continued intercellular flow in shrunken NCs.

392 **Tables S1 to S3**

393 **Table S1. Fly stocks used in this study, their source, and figures in which they appeared.**

Transgene name	Source*	Relevant to:
ubi>Pav::mCh	gift from Dr. Emmanuel Derivery	Figure 1
PCNA::GFP	gift from Dr. Eric Wieschaus	Figure 1, Figure S2
Resille::GFP/+; PCNA::GFP/pav::mCh	Lab stocks	Figure 1
Ecad:GFP	Lab stocks	Figure 1, Figure S1
sqh::mCh; *ubi>GFP::rok*	Lab stocks	Figure S6
UASp-F-tractin::TdTom	BDSC (58989)	Figure S6
Pdi::GFP	BDSC (6839)	Figure S7
TJ-Gal4; *H2A::GFP*, *GAP43::mCH*	Lab stocks	Figure 4
mat67; sqh::mCH; GFP::Clip170/Tm3	Lab stocks	Figure 1, Figure 3, Figure S2
w; sqhGFP, gap43mCh	Lab stocks	Figure S3
Resille::GFP	Lab stocks	Figure S3
mat67, Utr::GFP	Lab stocks	Figure S6
w; Utr-ABD::mCH, sqh(A20E21)::GFP (attP1)/Cyo	Lab stocks	Figure 1, Figure S2
sqh^1 *FRT/FM7; sqhTS::GFP/CyO*	Lab stocks	Figure 2†
ovoD FRT; hsFlp	Lab stocks	Figure 2†
y^1 v^1; P{TRiP.HMJ02093}attP40/CyO	BDSC (42527)	Figure 3, Figure 4, Figure S7‡

394

395 * BDSC: Bloomington *Drosophila* Stock Center; VDRC: Vienna *Drosophila* Resource Center.
396 †sqh^1 germline generated using the FLP-DFS technique by crossing sqh^1 *FRT/FM7; sqhTS::GFP/CyO* females to
397 *ovoD FRT; hsFlp* males and heat shocking sqh^1 *FRT/*ovo^D *FRT; CyO/hsFlp* embryos for 2 hours at 37°C for 3 -
398 4 days *(22)*. A control lacking heat shock verified the presence of the ovo^D allele.
399 ‡RhoGAP15B-RNAi knockdown flies were generated by crossing males of the shRNA line #42527 to virgin flies
400 carrying maternally-loaded GAL4 drivers with *mat67; sqh::mCH; GFP::Clip170/Tm3*.

401 **Table S2 | Measurement types and sample sizes used to generate the figures.**

Figure	Measurements	N	Number of egg chambers
1D	Deformation and projected area	4 cells	2
1E	Myosin COV; points are measurements at different timepoints	534 measurements from 4 cells	2
2C	Cell size over time	41 cells total	8
2I	Cell size over time	44 cells total	5
3F	Wave onset time	63 cells total	10
3I	Cell size over time	18 cells total	4
4E	Intercellular flow behaviors	WT: 6 events spanning 30 minutes; RhoGAP15B: 29 events spanning 54 minutes	2 (WT), 7 (RhoGAP15B)
4F	Intracellular flow behaviors	WT: 28 events spanning 239 minutes; RhoGAP15B: 82 events spanning 338 minutes	2 (WT), 7 (RhoGAP15B)
S1A	Length of NC cluster and oocyte	4	4
S1D	Cell sizes from FIJI and Imaris	39 measurements from 9 cells	4
S2B	Wave onset time	63 cells total	10
S2E	Size over time	30 cells total	8
S3B	COV of Sqh	534 measurements from 4 cells	2
S3C	COV of Resille	504 measurements from 5 cells	2
S5A	Ring canal diameter	370 ring canals	26
S5B	Nurse cell boundary position	9 egg chambers	9
S7B	Ring canal radii at stages 10-11	WT: 162 ring canals; RhoGAP15B: 144 ring canals	11 (WT), 10 (RhoGAP15B)

402

403
404 **Table S3 | Summary of initial conditions and parameters used in the mathematical model.**

Fixed			Optimized		
Layer	**# of cells**	**Initial volume***	**Parameter**	**Parameter range†**	**Best fit‡**
Oocyte	1	100	ρ	$[0.22, 1]$	0.55
1	4	9.00	r_1	$[0.11, 0.43]\ell_0$	0.37
2	6	6.61	r_2	$[0.11, 0.43]\ell_0$	0.40
3	4	5.07	r_3	$[0.13,0.40]\ell_0$	0.32
4	1	4.03	r_4	$[0.10, 0.30]\ell_0$	0.26

405 *In units of ℓ_0^3.
406 †Range of ring canal radii is given by the experimental average ±60% for each layer; unitless for ρ.
407 ‡Best fit parameters are those that result in smallest error as defined in the methods section.
408

409 **Movies S1 to S10**

410

411 **Movie S1**. Part I: Maximum intensity projection (MIP) of an egg chamber expressing *Ecad::GFP* to mark
412 germline cells' membranes. The shrinking NC cluster moves anteriorly (top) as cells transport their
413 cytoplasm into the growing posterior oocyte (bottom). Movie length: 4.5 hours; 64-second intervals.
414 Scale bar 50 μm, 1300x real time. Part II: Reflection-mode microscopy of an egg chamber showing
415 intercellular movement of NC cytoplasm (cyan) through ring canals (arrows) towards the oocyte
416 (positioned left). Movie length: 39 seconds, with 0.5-second intervals. Scale bar 20 μm, 10x real time.

417

418 **Movie S2.** MIP generated from 4D live imaging of an egg chamber expressing *Sqh::mCH* (red) to label
419 myosin and *PCNA::GFP* (cyan) a to mark the cells' nuclei. Onset of NC dumping and transport of most
420 of NC volume occurs as NC shrink uniformly without undergoing cell shape deforming contractions.
421 Nonuniform cell contractions commence at 1 hour, 29 minutes (arrow), when ~75% of NC volume is
422 transported. Movie length: 2 hours 20 minutes; 20-second time points. Scale bar 50 μm, 400x real time.

423

424 **Movie S3.** Heat map of an average intensity projection generated from 4D live imaging of an egg
425 chamber expressing *Sqh::GFP*. White line indicates position of NC-oocyte boundary at the onset of NC
426 dumping. As NC unfolds, NC actomyosin cortical pattern changes from a uniform to a non-uniform and
427 dynamic pattern, coincident with onset of contractile NC shape deformations. Movie length: 54 minutes;
428 20-second time points. Scale bar 50 μm, 480x real time.

429

430 **Movie S4.** Animation of NC dumping on the 16-cell network generated using matplotlib in Python,
431 starting with experimentally determined sizes and showing the evolution of cell radii according to the
432 simulation best fit. Ring canals are red when flow proceeds towards the oocyte; blue canals indicate
433 backwards flow. Animation is approximately 2700x real time.

434 **Movie S5.** MIP generated from 4D live imaging of a sqh^1 egg chamber stained with CellMask (magenta).
435 Despite a reduction of ~90% of Sqh mRNA and protein levels, the first (cyan arrows) and second (red
436 arrows) NC layers nonetheless empty their contents into the oocyte as NC dumping unfolds. Transport is
437 however incomplete, leading to a dumpless phenotype. Movie length: 2.5 hours; 30-second time points.
438 Scale bar 50 μm, 720x real time.

439

440 **Movie S6.** MIPs from 4D live imaging of egg chambers expressing *Sqh::mCH* (red) and *Clip170::GFP*
441 (cyan) to mark cells' myosin and cytoplasm, respectively, highlighting the diversity of actomyosin wave-

like behaviors. Left movie shows an example of myosin rings travelling between the cell's poles (white arrow); right movie shows examples of a colliding myosin wave fronts (yellow arrow) and a rotating cortical band (gray arrow). Movie lengths: 83 minutes with 28-second time points (left); 51 minutes with 17-second time points (right). Scale bar 50 μm; left movie 670x real time, right movie 410x real time.

Movie S7. MIP generated from 4D live imaging of an egg chamber expressing *Utr::GFP* (cyan) and *F-tractin::TdTom* (magenta), showing similar wave-like dynamics as myosin. Movie length: 2 hours, 53 minutes; 28-second time points. Scale bar 50 μm, 670x real time.

Movie S8. MIP generated from 4D live imaging of egg chamber with a RhoGAP15B depleted germline, expressing *Clip170::GFP* (cyan, left) and *Sqh::mCH* (red, right) to mark cells' myosin and cytoplasm. RhoGAP15B knockdowns exhibit disrupted actomyosin dynamics and do not complete NC dumping, resulting in a remnant NC cluster and a dumpless phenotype. Movie length: 113 minutes; 35-second time points. Scale bars 50 μm, 840x real time.

Movie S9. Left: Live imaging of one slice of an egg chamber, obtained using reflection-mode microscopy to capture cytoplasmic movement (cyan) and stained with CellMask (white) to show cell membranes. As dumping unfolds, cells deform dynamically. Inset: oocyte-NC cluster boundary (yellow line) at NC dumping onset. Movie length: 24 minutes; 10-second time points. Scale bar 50 μm. Right: Blow-up of one slice of a single NC; contractile shape deformations enable continuous cytoplasmic flow past nuclei in shrunken NCs, enabling complete dumping. Movie length: 24 minutes; 10-second time points. Scale bar 20 μm. Both movies are 250x real time.

Movie S10. Part I: Live imaging movie showing a single slice of a RhoGAP15B depleted egg chamber during NC dumping, captured using reflection mode microscopy to highlight the NCs' cytoplasm (cyan). Intracellular flow in RhoGAP15B knockdowns lacks the persistent radial motions around NC nuclei that are observed in WT, instead exhibiting short-lived and erratic protrusions. Part II: reflection-mode microscopy movie of the boxed region highlights rapid reversal of flow direction from normal anterior-to-posterior (A-to-P) to abnormal P-to-A flow through the ring canals (yellow arrow under the ring canal indicates direction). Movie lengths: 170 seconds; 4.6-second intervals, and 298 seconds; 1.4-second intervals. Scale bars 20 μm, 90x real time and 30x real time.

References

1. J. Schindelin *et al*. Fiji: an open-source platform for biological-image analysis. *Nat. Methods* ***9***, 676-682 (2012).
2. Bitplane Inc. Imaris Version 9.3.0, imarisxt. Zurich, Switzerland
3. MATLAB, 2018. *9.5.0.1033004 (R2018b)*, Natick, Massachusetts: The MathWorks Inc.
4. Y. Shimada, M. K. R. Mahala Burn, L. Niwa, L. Cooley. Reversible response of protein localization and microtubule organization to nutrient stress during *Drosophila* early oogenesis. *Dev Biol*. ***355***, 250-262 (2011).
5. H. Lin H, A.C. Spradling, Germline stem cell division and egg chamber development in transplanted *Drosophila* germaria. *Dev. Biol*. ***159***, 140-152 (1993).
6. K. Doubrovinski, M. Swan, O. Polyakov, E. F. Wieschaus. Measurement of cortical elasticity in *Drosophila melanogaster* embryos using ferrofluids. *Proc. Natl. Acad. Sci. U.S.A*. ***114***, 1051-1056 (2017).
7. D.R. Merrit, F. Weinhaus, The pressure curve for a rubber balloon. *Am. J. Phys*. ***46***, 976-977 (1978).
8. A.R. Bausch, K. Kroy. A bottom-up approach to cell mechanics. *Nat. Phys*. ***2***, 231-238 (2006).
9. H.M. James, E. Guth. Theory of the Elastic Properties of Rubber. *J. Chem. Phys*. ***11***, 455 (1943).
10. E. Verron, R.E. Khayat, A. Derdouri, B Peseux, Dynamic inflation of hyperelastic spherical membranes. *J. Rheol*. ***43***, 1083-1097 (1999).
11. R. Vargas-Pinto, H. Gong, A. Vahabikashi, M. Johnson. The effect of the endothelial cell cortex on atomic force microscopy measurements. *Biophys. J*. ***105***, 300-309 (2013).
12. T. Lecuit, P. Lenne. Cell surface mechanics and the control of cell shape, tissue patterns and morphogenesis. *Nat. Rev. Mol. Cell Biol*. ***8***, 633-644 (2007).
13. D.J. Acherson, *Elementary Fluid Dynamics* (Clarendon Press, Oxford, 1990).
14. A. Diz-Muñoz, D. A. Fletcher, O. D. Weiner. Use the force: Membrane tension as an organizer of cell shape and motility. *Trends Cell Biol*. ***23***, 47-53 (2013).
15. C.E. Morris, U. Homann. Cell surface area regulation and membrane tension. *J. Membr. Biol*. ***179***, 79-102 (2001).
16. J. Chlasta *et al*. Variations in basement membrane mechanics are linked to epithelial morphogenesis. *Development* ***144***, 4350-4362 (2017).
17. J.J. Thottacherry *et al*. Mechanochemical feedback control of dynamin independent endocytosis modulates membrane tension in adherent cells. *Nat. Commun*. ***9***, 4217 (2018).
18. N.P. Gonzalez, J. Tao, N. D. Rochman, D. Vig, E. Chiu, D. Wirtz, S.X. Sun. Cell tension and mechanical regulation of cell volume. *Mol. Biol. Cell*. ***29***, 2591-2600 (2018).

506 19. J. Imran Alsous, P. Villoutreix, A.M. Berezhkovskii, S.Y. Shvartsman, Collective growth in a small
507 cell network. *Curr. Biol.* ***27***, 2670-2676 (2017).
508 20. H.O. Gutzeit, The role of microfilaments in cytoplasmic streaming in *Drosophila* follicles. *J. Cell Sci.*
509 ***80***, 159-169 (1986).